

1 **Impact of topography on black carbon transport to the southern Tibetan**
2 **Plateau during pre-monsoon season and its climatic implication**

3 ¹Meixin Zhang, ¹Chun Zhao*, ^{2,3}Zhiyuan Cong, ¹Qiuyan Du, ¹Mingyue Xu, ¹Yu Chen, ⁴Ming
4 Chen, ¹Rui Li, ¹Yunfei Fu, ¹Lei Zhong, ^{3,5}Shichang Kang, ⁶Delong Zhao, ⁶Yan Yang
5
6

7 ¹School of Earth and Space Sciences, University of Science and Technology of China, Hefei,
8 China

9 ²Key Laboratory of Tibetan Environment Changes and Land Surface Processes, Institute of
10 Tibetan Plateau Research, Chinese Academy of Sciences (CAS), Beijing 100101, China

11 ³CAS Center for Excellence in Tibetan Plateau Earth Sciences, Institute of Tibetan Plateau
12 Research, CAS, Beijing 100101, China

13 ⁴National Center for Atmospheric Research, Boulder, CO, USA

14 ⁵State Key Laboratory of Cryosphere Science, Northwest Institute of Eco-Environment and
15 Resources, CAS, Lanzhou 730000, China

16 ⁶Beijing Weather Modification Office, Beijing 100101, China
17

18 Manuscript for submission to Atmos. Chem. Phys.
19
20

21 *Corresponding author: Chun Zhao (chunzhao@ustc.edu.cn)
22
23

24 **Key points:**

25 1. The black carbon (BC) transport across the Himalayas can overcome a majority of mountain
26 ridges, but the valley transport is much more efficient during the pre-monsoon season.

27 2. The complex topography results in stronger overall crossing-Himalayas transport during the
28 study period primarily due to the strengthened efficiency of near-surface meridional transport
29 towards the TP, enhanced wind speed at some valleys, and deeper valley channels associated
30 with larger transported BC mass volume.

31 3. The complex topography generates 50% higher transport flux of BC across the Himalayas
32 and 30-50% stronger BC radiative heating in the atmosphere up to 10 km over the Tibetan
33 Plateau (TP) than that with the smoother topography, which implies that global climate models
34 with relatively coarse resolution may introduce significant negative biases in estimating BC
35 radiative forcing over the TP due to smooth topography.

36 4. The different topography also leads to different distributions of snow cover and BC forcing
37 in snow over the TP.
38

39 **Abstract**

40 Most of previous modeling studies about black carbon (BC) transport and impact over the
41 Tibetan Plateau (TP) conducted simulations with horizontal resolutions coarser than 10 km that
42 may not be able to resolve well the complex topography of the Himalayas. In this study, the
43 two experiments covering entire Himalayas with the Weather Research and Forecasting Model
44 coupled with chemistry (WRF-Chem) at the horizontal resolution of 4 km but with two
45 different topography datasets (4-km complex topography and 20-km smooth topography) are
46 conducted for pre-monsoon season (April, 2016) to investigate the impacts of topography on
47 modeling the transport and distribution of BC over the TP. Both experiments show evident
48 accumulation of aerosols near the southern Himalayas during the pre-monsoon season,
49 consistent with the satellite retrievals. The observed episode of high near-surface BC
50 concentration at the station near the Mt. Everest due to heavy biomass burning near the
51 southern Himalayas is well captured by the simulations. The simulations indicate that the
52 prevailing up-flow across the Himalayas driven by the large-scale westerly and small-scale
53 southerly circulations during the daytime is the dominant transport mechanism of South Asian
54 BC into the TP, and is much stronger than that during the nighttime. The simulation with 4-km
55 topography resolves more valleys and mountain ridges, and shows that the BC transport across
56 the Himalayas can overcome a majority of mountain ridges but the valley transport is more
57 efficient. The complex topography results in stronger overall crossing-Himalayas transport
58 during the simulation period primarily due to the strengthened efficiency of near-surface
59 meridional transport towards the TP, enhanced wind speed at some valleys, and deeper valley
60 channels associated with larger transported BC mass volume. This results in 50% higher
61 transport flux of BC across the Himalayas and 30-50% stronger BC radiative heating in the
62 atmosphere up to 10 km over the TP from the simulation with 4-km complex topography than
63 that with 20-km smoother topography. The different topography also leads to different
64 distributions of snow cover and BC forcing in snow. This study implies that global climate
65 models generally with even coarser resolutions than 20 km and therefore relatively smoother
66 topography may introduce significant negative biases in estimating light absorbing aerosol
67 radiative forcing over the TP.

68

69

70

71

72

73 1. Introduction

74 The Tibetan Plateau (TP) is the highest plateau in the world with an average elevation
75 over 4 km and an area of approximately $2.5 \times 10^6 \text{ km}^2$, known as the world's third pole (Qiu,
76 2008), and its enormous dynamic and thermal effects have a huge impact on large-scale
77 atmospheric circulation through the energy exchange with the atmosphere especially the
78 troposphere, such as Asian monsoon (e.g., Ye and Wu, 1998; Duan and Wu, 2005; Wu et al.,
79 2007, 2012a; Boos and Kuang, 2013; Chen and Bordoni, 2014; He et al., 2019; Zhao et al.,
80 2019). In addition, the glacial melting water of TP is one of the important sources of water
81 resources of the Indus River, Ganges River, Yangtze River, and Yellow River in Asia (e.g.,
82 Singh and Bengtsson, 2004; Barnett et al., 2005; Immerzeel et al., 2010; Lutz et al., 2014).
83 Previous studies found aerosols in the atmosphere over/around the TP could change the
84 regional climate of Asia (e.g., Qian et al., 2011, 2015; Lau et al., 2017, 2018). Model
85 simulations showed that the absorptive aerosols changed the surface radiative flux over the TP
86 by $5\text{-}25 \text{ W m}^{-2}$ during the pre-monsoon season in April and May and led to the changes in
87 summer monsoon circulations (Qian et al., 2011). Meanwhile, aerosol may affect the
88 atmosphere by modulating the vertical structure of cloud and precipitation around the TP, and
89 thus change the distribution of atmospheric latent heat around the TP, which is the main driving
90 force of regional atmosphere circulations (e.g., Li et al., 2010, 2017, 2019). Moreover, when
91 absorbing aerosols settle on the snow-covered areas, they will blacken the surface of snow
92 cover and glacier to a large extent (e.g., Hansen and Nazarenko, 2004; Ramanathan and
93 Carmichael, 2008; Lau et al., 2010, 2018; Lee et al., 2013; Zhang et al., 2017, 2018), reduce
94 the snow albedo so as to absorb more solar radiation and cause the consequences of accelerated
95 melting (e.g., Ramanathan et al., 2007; Ming et al., 2009; Yasunari et al., 2010; Ji et al., 2015;
96 Zhang et al., 2015). According to the Intergovernmental Panel on Climate Change Fifth
97 Assessment Report (IPCC AR5), the radiative forcing caused by the important component of
98 absorbing aerosols, black carbon (BC), on the surface snow is 0.04 W m^{-2} ($0.02\text{-}0.09 \text{ W m}^{-2}$)
99 on global average, and the regional forcing (such as over the Arctic and the Himalayas) can be
100 considerably large.

101 The TP is surrounded by various sources of pollutants. Over the South of TP, previous
102 studies have suggested that South Asia was the main source of pollutants transported to the
103 plateau (e.g., Cong et al., 2009, 2015a, b; Kopacz et al., 2011; Lu et al., 2012; Zhao et al., 2013;
104 Wang et al., 2015; Zhang et al., 2015; Kang et al., 2016, 2019; Li et al., 2016; Chen et al.,
105 2018). A huge blanket or layer of "haze" composes of light-absorbing carbonaceous aerosol

106 particles that often erupts in the pre-monsoon season over South Asia and has a significant
107 influence on the plateau (e.g., Prasad and Singh, 2007; Engling and Gelencser, 2010). Among
108 them, biomass burning emission reaching the maximum in pre-monsoon season over South
109 Asia is one of the dominant sources (e.g., Cong et al., 2015b). Many studies investigated the
110 transport mechanisms of South Asian pollutants to the TP and found that the pollutants
111 transported across the Himalayas were mainly due to the combination of large-scale circulation
112 and regional wind (e.g., Hindman and Upadhyay, 2002; Cao et al., 2010; Dumka et al., 2010;
113 Marinoni et al., 2010; Cong et al., 2015a; Kang et al., 2016; Lüthi et al., 2015; Zhang et al.,
114 2017). Cong et al. (2015b) suggested that strong large-scale westerly and local small-scale
115 mountain-valley wind passed through western Nepal, northwest India and Pakistan (i.e.,
116 southern Himalayas) in the pre-monsoon season. Dumka et al. (2010) and Kang et al. (2016)
117 inferred from the trajectory analysis that long-distance transport from Africa and Europe may
118 also affect the BC concentration of Himalayas in addition to the influence of regional pollution.
119 The synoptic troughs and ridges were also found favoring the transport of pollutants into the
120 TP from South Asia (Lüthi et al., 2015).

121 Although previous studies have confirmed the transport of pollutants across the Himalayas,
122 the complex topography of Himalayas complicates transport mechanisms. On one hand, Cao
123 et al. (2010) revealed that the Himalayas acted as a huge barrier to the transport of a large
124 amount of BC over the plateau based on model simulations. On the other hand, some studies
125 found that the valleys across the Himalayas served as channels for efficient transport of
126 pollutants (e.g., Hindman and Upadhyay, 2002; Marinoni et al., 2010). Marinoni et al. (2010)
127 analyzed the observation of wind at a station of the southern Himalayas and found that a distinct
128 valley wind system with the prominent southerly continuously transported pollutants to the
129 plateau. Most of these studies used observations and back-trajectory models to demonstrate the
130 transport pathways of pollutants to the TP, which cannot explicitly reveal the transport
131 mechanisms underneath, in particular quantifying the impacts of complex topography.

132 A few of modeling studies investigated the pollutant transport mechanisms using 3-D
133 chemical transport models (e.g., Kopacz et al., 2011; Liu et al., 2015; Zhang et al., 2017; Yang
134 et al., 2018). However, most of them simulated transport processes at relatively coarse
135 horizontal resolutions (e.g., 20-100 km), which cannot resolve well the complex topography of
136 Himalayas. It is noteworthy that studies about the aerosol climatic impact over the TP also used
137 climate models at relatively coarse horizontal resolutions (e.g., Flanner and Zender, 2005;
138 Menon et al., 2010; Kopacz et al., 2011; Qian et al., 2011, 2015; He et al., 2014; Zhang et al.,
139 2015; Ji et al., 2016). So far, there is only one study that used a chemical transport model at a

140 horizontal resolution of sub-10 km to investigate pollutant transport mechanisms over the
141 eastern Himalayas (Cao et al., 2010). Furthermore, none of studies assessed quantitatively the
142 impacts of topography on modeling the pollutant transport across the Himalayas and hence on
143 estimating aerosol distribution and radiative forcing over the TP.

144 In order to examine the potential impacts of complex topography on pollutant transport
145 across the Himalayas over the TP, this study conducts multiple experiments with the Weather
146 Research and Forecasting Model coupled with chemistry (WRF-Chem, Grell et al., 2005;
147 Skamarock et al., 2008). The WRF-Chem model is selected because it includes the interaction
148 between meteorology and aerosol and is widely used for regional modeling of aerosol and its
149 climatic impact (e.g., Cao et al., 2010; Zhao et al., 2010, 2011, 2012, 2014; Wu et al., 2013;
150 Gao et al., 2014; Huang et al., 2015; Fan et al., 2015; Feng et al., 2016; Zhong et al., 2017;
151 Sarangi et al., 2019; Liu et al., 2020). The model has also been used to investigate the aerosol
152 transport and climatic impact over the Himalayas region (e.g., Feng et al., 2016; Cao et al.,
153 2010; Sarangi et al., 2019). The model is suitable for simulations at hydrostatic and non-
154 hydrostatic scales and thus can be used for investigating the impacts of resolution-dependent
155 feature, such as topography, on modeling results. In particular, the meteorological part of the
156 model (WRF) has been systematically evaluated and used to investigate the impacts of
157 resolutions on simulations of moisture transport and climate over the Himalayas region (e.g.,
158 Shi et al., 2008; Karki et al., 2017; Lin et al., 2018; Zhou et al., 2017, 2018; Wang et al., 2020).
159 All of these previous studies with the model lay the foundation for this modeling study.

160 Two experiments with different topography representations are conducted to investigate
161 the impacts of topography complexity on the pollutant transport across the Himalayas and the
162 resulting radiative forcing over the TP. The simulations are conducted for April 2016 in pre-
163 monsoon season, because South Asia is seriously polluted during this period and the pollutants
164 transported to the TP during the period may have significant impacts on Asian monsoon system
165 (e.g., Lau et al., 2006a, b; Ding et al., 2009; Kuhlmann and Quaas, 2010; Qian et al., 2011,
166 2015). In addition, the observed concentration of BC at the observation station besides Mt.
167 Everest shows an evident pollution episode from April 5th to 16th of 2016, deserving the
168 investigation of the transport mechanisms. The rest of the paper is organized as follows. Section
169 2 describes briefly the WRF-Chem model, the physics parameterizations, and the model
170 configuration for this study, followed by a description of data for evaluation. The series of
171 numerical experiments at different resolutions are analyzed in Section 3. The findings are then
172 summarized and discussed in Section 4 and 5.

173

174 **2. Methodology**

175 **2.1 Model and experiments**

176 2.1.1 WRF-Chem model

177 In this study, the version of WRF-Chem updated by University of Science and Technology
178 of China (USTC version of WRF-Chem) is used. This USTC version of WRF-Chem includes
179 some additional capabilities such as the diagnosis of radiative forcing of aerosol species, land
180 surface coupled biogenic volatile organic compound (VOC) emission, aerosol-snow
181 interaction compared with the publicly released version (Zhao et al., 2013a, b, 2014, 2016; Hu
182 et al., 2019; Du et al., 2020). The Model for Simulating Aerosol Interactions and Chemistry
183 (MOSIAC) (Zaveri et al., 2008) and the Carbon Bond Mechanism-Z (CBM-Z) gas phase
184 mechanisms (Zaveri and Peters, 1999) are selected. The MOSAIC aerosol scheme uses an
185 approach of segmentation to represent aerosol size distribution with four or eight discrete size
186 bins (Fast et al., 2006). It consists of a range of physical and chemical processes such as
187 nucleation, condensation, coagulation, aqueous phase chemistry, and water uptake by aerosol.
188 The parameterization of dry deposition of aerosol mass and number is according to the method
189 of Binkowski and Shankar (1995), including particle diffusion and gravitational effects.
190 Aerosol-cloud interactions were included in the model by Gustafson et al. (2007) for
191 calculating the activation and re-suspension between dry aerosols and cloud droplets. The wet
192 removal of grid-resolved stratiform clouds/precipitation includes two aspects, namely in-cloud
193 removal (rainout) and below-cloud removal (washout) by Easter et al. (2004) and Chapman et
194 al. (2009), respectively. Aerosol optical properties such as single scattering albedo (SSA) and
195 scattering asymmetry and so on are calculated at each model grid through the function of
196 wavelength. The shortwave (SW) and longwave (LW) refractive indices of aerosols use the
197 Optical Properties of Aerosols and Clouds (OPAC) data set (Hess et al., 1998), with a detailed
198 description of the computation of aerosol optical properties can be found in Barnard et al. (2010)
199 and Zhao et al. (2013a). For both short wave and long wave radiation, aerosol radiation
200 feedback combined with the Rapid Radiative Transfer Model (RRTMG) (Mlawer et al., 1997;
201 Iacono et al., 2000) was implemented by Zhao et al. (2011). For the diagnosis of the optical
202 properties and direct radiative forcing of various aerosol species in the atmosphere, the method
203 described by Zhao et al (2013a) is adopted. The radiative forcing of light absorbing aerosol in
204 surface snow is estimated with the Snow, Ice, and Aerosol Radiative model (SNICAR)
205 (Flanner and Zender, 2005) in the land surface scheme as introduced by Zhao et al. (2014).

206 More details about the coupling between the WRF-Chem and SNICAR models can be found
207 in Zhao et al. (2014).

208

209 2.1.2 Numerical experiments

210 In this study, the WRF-Chem simulations are performed with two nested domains (one-
211 way nesting), one outer domain at 20-km horizontal resolution with 350×250 grid cells (62°E
212 -112°E, 1°N -38°N) and one inner domain at 4-km horizontal resolution with 400×300 grid
213 cells (75°E -92°E, 23°N -35°N) (Fig. 1). The inner domain roughly covers the entire Himalayas.
214 The WRF-Chem simulations conducted in this study use the terrain following coordinate
215 (Skamarock et al., 2008). To resolve the vertical structure of transport across the Himalayas,
216 the simulations are configured with 54 vertical layers and denser layers near the surface. For
217 example, averaged over a region (26°N-28°N, 76°E-80°E) near the southern Himalayas, there
218 are about 17 layers below 2 km above the ground (Fig. 2). The goal of this study is to investigate
219 the impacts of different representations of topography on the transport of BC across the
220 Himalayas. Therefore, besides this control experiment, one sensitivity (idealized) experiment
221 is also conducted with the same configuration as the control one except that the terrain height
222 of the inner domain at 4-km resolution is prescribed to follow that at 20-km resolution similar
223 as previous studies (e.g., Shi et al., 2008; Wu et al., 2012b; Lin et al., 2018). More specifically,
224 the sensitivity experiment applies a single value for each nested 5×5 grids over the inner
225 domain as the corresponding grid of 20 km over the outer domain. The two experiments are
226 referred to the simulations with complex and smooth topography, respectively, hereafter.

227 Fig. 3 shows the spatial distribution of terrain height over the inner domain with complex
228 (4-km dataset) and smooth (20-km dataset) topography. It is evident that the terrain is much
229 smoother from the 20-km dataset than from the 4-km dataset. The mountain ridges and valleys
230 can be resolved to some extent in the 4-km dataset but mostly missed or underestimated at 20-
231 km. The probability distributions of terrain height from the 20-km and 4-km datasets (Fig. S1
232 in the supporting material) show that the difference between the two datasets is small for the
233 terrain height lower than ~4.5 km but is significant for the terrain height above ~4.5 km. The
234 difference of results from the two experiments over the inner domain is analyzed as the impacts
235 of topography representations. Therefore, all the results shown below are from the simulations
236 of the inner domain at 4-km resolution with different topography if not otherwise stated. It is
237 noteworthy that this study focuses on understanding the impact of complex topography
238 resolved by 4 km instead of the difference between 4-km and 20-km simulations. Prescribing

239 the topography at 4 km following the 20-km resolution distribution is just one way to smooth
240 the topography. In fact, the sensitivity experiment at 4-km resolution with the topography from
241 the one-degree resolution dataset is also conducted, and the result is consistent. In addition,
242 although the topography at 4-km resolution resolves much better topography of Himalayas than
243 that at 20-km resolution, it still cannot fully resolve the complexity of topography of Himalayas.
244 The higher resolution (e.g., 1 km or sub-1 km) may be needed. Previous studies have found
245 that the simulations at the resolutions between 1 km and 4 km can produce generally consistent
246 features, but the simulation at 1 km with better representation of topography can produce a
247 little better meteorological field compared to the observations (e.g., Karki et al., 2017). One
248 sensitivity experiment at 1.5-km resolution is also conducted in this study and found the
249 difference between the simulations at 1.5-km and 4-km resolutions is relatively small. However,
250 it should be noted that the simulation at 1.5-km resolution is only conducted covering a much
251 smaller region for a shorter period due to the computational cost. The experiment at 4-km
252 instead of 1.5-km resolution is conducted finally for the study region and period due to the
253 balance of resolving the complex topography to some extent and affordable computational cost.

254 The simulations are conducted for March 29th-April 20 of 2016 for the reason as discussed
255 in the introduction. The results of April 1th-20th are analyzed for the observed pollution episode
256 to allow a few days spin-up for chemical initial condition. The meteorological initial and lateral
257 boundary conditions are derived from the European Centre for Medium-Range Weather
258 Forecasts (ECMWF) reanalysis data at $0.5^{\circ} \times 0.66^{\circ}$ horizontal resolution and 6 h temporal
259 intervals (ERA-Interim dataset). The modeled u and v component wind, atmospheric
260 temperature, and geopotential height over the outer domain are nudged towards the reanalysis
261 data with a nudging timescale of 6 h following previous studies (e.g., Stauffer and Seaman,
262 1990; Seaman et al., 1995; Liu et al., 2012; Zhao et al., 2014; Karki et al., 2017; Hu et al., 2016,
263 2020). Spectral nudging method is applied to balance the performance of simulation at the large
264 and small scales (Liu et al., 2012), and only to the layers above the planetary boundary layer
265 (PBL) with nudging coefficients of $3 \times 10^{-4} \text{ s}^{-1}$. A wave number of three is selected for both
266 south-north and west-east directions. Please note that the choices of nudging coefficients and
267 wave numbers for spectral nudging in this study are empirical. The purpose of nudging is to
268 simulate reasonably large-scale feature so that small-scale impacts from the complex
269 topography can be focused. Therefore, the modeling sensitivity to these choices is not tested in
270 this study. The results show that the simulations with nudging method can reproduce the large-

271 scale circulation at 700 hPa and higher over the outer domain compared to the reanalysis dataset
272 with the spatial correlation coefficient of 0.96-0.98.

273 The Mellor-Yamada-Nakanishi-Niino (MYNN) planetary boundary layer scheme
274 (Nakanishi and Niino, 2006), Community Land Model (CLM) land surface scheme (Oleson et
275 al., 2010), Morrison 2-moment microphysics scheme (Morrison et al., 2009), Kain-Fritsch
276 cumulus scheme (Kain, 2004), and Rapid Radiative Transfer Model (RRTMG) longwave and
277 shortwave radiation schemes (Iacono et al., 2000) are used in this study. The chemical initial
278 and boundary conditions are provided by a quasi-global WRF-Chem simulation for the same
279 time period to include long-range transported chemical species. The quasi-global WRF-Chem
280 simulation is performed at $1^{\circ}\times 1^{\circ}$ horizontal resolution using a quasi-global channel
281 configuration with 360×130 grid cells ($180^{\circ}\text{W}-180^{\circ}\text{E}$, $60^{\circ}\text{S}-70^{\circ}\text{N}$). More details about the
282 general configuration of quasi-global WRF-Chem simulation can be found in Zhao et al.
283 (2013b) and Hu et al. (2016). The detailed configuration of WRF-Chem experiments is
284 summarized in Table 1. Due to the lack of publicly available in-situ observations, this study
285 does not tend to evaluate systematically the simulated meteorological fields over the Himalayas
286 region. However, as shown in Table 1, the choice of physical parameterizations in this study
287 follows that of one previous study (Karki et al., 2017) that evaluated systematically the WRF
288 simulation for one entire year over the Himalayas region. Their results showed that the WRF
289 simulation at convection-permitting scale could generally capture the essential features of
290 meteorological fields such as precipitation, temperature, and wind over the Himalayas region.
291 Therefore, the WRF-Chem simulations in this study are reliable to investigate the impacts of
292 topography over the Himalayas region.

293

294 2.1.3 Emissions

295 Anthropogenic emissions for outer and inner simulation domains are obtained from the
296 Hemispheric Transport of Air Pollution version-2 (HTAPv2) at $0.1^{\circ}\times 0.1^{\circ}$ horizontal resolution
297 and a monthly temporal resolution for year 2010 (Janssens-Maenhout et al., 2015), except that
298 emissions of East Asia are from the MIX Asian anthropogenic emission inventory at $0.1^{\circ}\times 0.1^{\circ}$
299 horizontal resolution for 2015 (Li et al., 2017). Biomass burning emissions are obtained from
300 the Fire Inventory from National Center for Atmospheric Research (FINN) with hourly
301 temporal resolution and 1-km horizontal resolution (Wiedinmyer et al., 2011) for the
302 simulation period, and are vertically distributed following the injection heights suggested by
303 Dentener et al. (2006) from the Aerosol Comparison between Observations and Models

304 (AeroCom) project. Sea-salt emission follows Zhao et al. (2013b), which includes correction
305 of particles with radius less than $0.2 \mu\text{m}$ (Gong, 2003) and dependence of sea-salt emission on
306 sea surface temperature (Jaeglé et al., 2011). The vertical dust fluxes are calculated with the
307 Georgia Tech/Goddard Global Ozone Chemistry Aerosol Radiation and Transport (GOCART)
308 dust emission scheme (Ginoux et al., 2001), and the emitted dust particles are distributed into
309 the MOSAIC aerosol size bins following a theoretical expression based on the physics of scale-
310 invariant fragmentation of brittle materials derived by Kok (2011). More details about the dust
311 emission scheme coupled with MOSAIC aerosol scheme in WRF-Chem can be found in Zhao
312 et al. (2010, 2013b).

313 As shown in Fig. 1, anthropogenic fossil fuel emissions of BC are high over Northeast
314 India. The fossil fuel BC emissions over Nepal, the country nearby the southern Himalayas,
315 are relatively low. Instead, biomass burning emissions of BC are extremely high in Nepal and
316 Northwest India (South Himalayas, 26°N - 29°N). Averaged over the South Himalayas of inner
317 domain that may significantly affect the pollutant transport into the TP, the biomass burning
318 emissions of BC are much higher than its anthropogenic fossil fuel emissions, particularly for
319 the pollution episode (Fig. 4). The anthropogenic BC emissions are set constant through April,
320 while biomass burning emissions show a strong fire event in April 5-16. During the event, the
321 biomass burning BC emissions can be a factor of 2 of the anthropogenic fossil fuel BC
322 emissions over South Himalayas.

323

324 **2.2 Dataset**

325 Three datasets are used to compare with the modeling results to demonstrate the pollutant
326 episode and spatial distribution. One is from the Moderate Resolution Imaging
327 Spectroradiometer (MODIS) instruments on Aqua and Terra satellites. The MODIS Aerosol
328 Product monitors the ambient aerosol optical thickness over the oceans globally and over the
329 continents. Daily Level 2 Aerosol Optical Depth (AOD) at 550 nm products with the spatial
330 resolution of $10 \text{ km} \times 10 \text{ km}$ (at nadir) from both Aqua and Terra are applied. When compared
331 with the modeling results, the simulations are sampled at the satellite overpass time and
332 location. The second one is from the Aerosol Robotic Network (AERONET) (Holben et al.,
333 1998) that has ~ 100 similar globally distributed sun and sky scanning ground-based automated
334 radiometers, which provide measurements of aerosol optical properties throughout the world
335 (Dubovik and King, 2000; Dubovik et al., 2002). In this study, AERONET measured AOD at
336 675 nm and 440 nm from two sites over the TP, QOMS_CAS site (86.95°E , 28.36°N) and
337 NAM_CO site (90.96°E , 30.77°N) are used to derive the AOD at 550 nm (using the Angström

338 exponent) for comparison with modeling results at 550 nm. All of the retrievals of AOD are at
339 quality level 2, and the uncertainty of AOD measurements is about 0.01 (Holben et al., 2001).
340 In this study, the available data in April 2016 are used to evaluate the modeling results during
341 the same period.

342 The third one is the measurement of near-surface BC mass concentration collected during
343 the simulation period for April 4-20 of 2016 at the Qomolangma Station for Atmospheric and
344 Environmental Observation and Research (QOMS, 86.95°E, 28.36°N) which is located at the
345 northern slope of the Mt. Everest, about 4276 meters above sea level. The BC mass
346 concentration is measured with the widely-used instrument Aethalometer (AE-33) that can
347 provide real-time BC mass concentration measurements. The calibration of air flow is routinely
348 conducted to maintain the data quality. The instrument estimates the BC mass concentration
349 based on the optical method through measuring the reduction in light intensity induced by BC.
350 The method assumes that the relationship between attenuation and BC surface loading is linear
351 for low attenuation values. However, this relationship becomes nonlinear when the attenuation
352 values are high due to a filter saturation effect, which may lead to underestimation of the high
353 BC concentration. The detection limit of AE-33 instrument is 5 ng/m³, and the uncertainty is
354 estimated to be within 10% (e.g., Chen et al., 2018; Bansal et al., 2019; Kant et al., 2019). The
355 dataset of BC mass concentration used in this study was reported by Chen et al., (2018), where
356 more details about the measurements can be found.

357

358 **3. Results**

359 **3.1 Spatial distribution of BC around the TP**

360 Figure 5 shows the spatial distributions of column integrated BC mass within the inner
361 domain from the simulations at 4-km resolution with complex and smooth topography
362 averaged for April 1-20, 2016, and the difference between the two is also shown. For both
363 experiments, the Himalayas is an apparent boundary line for the distribution of BC with a sharp
364 gradient across the Himalayas. The high BC mass loading exists near the southern Himalayas
365 reaching over 10 mg/m², which is largely contributed by the biomass burning emissions during
366 the period (Fig. 4), while the value reduces significantly to less than 0.4 mg/m² over the TP.
367 The BC mass loading near the central and eastern Himalayas is higher than that near the
368 western Himalayas. In general, the column BC mass loading from the simulation with complex
369 topography is higher over the TP and lower over the region to the south of Himalayas compared
370 with the smooth topography, reflecting the stronger transport of BC from the source region to

371 the Himalayas and TP due to the complex topography (see the discussion in Section 3.2). Figure
372 6 displays the spatial distributions of AOD from the MODIS retrievals and the simulations at
373 4 km with two different topography averaged for April 1-20, 2016. In general, both simulations
374 reproduce the overall spatial distribution of AOD, with the large values near the southern
375 Himalayas, consistent with the BC mass loading. In addition, both the simulations and satellite
376 retrievals show higher AOD near the central and eastern Himalayas than that near the western
377 Himalayas during the study period. The difference between the simulations and retrievals may
378 be partly related to the uncertainties in emissions particularly for biomass burning emissions.
379 Other than intense emissions, the wind circulation around the TP may also play an important
380 role in accumulating BC near the southern Himalayas. Because of the block of Himalayas, the
381 wind circulation at 500 hPa is divided into two branches as westerly and northwesterly. Both
382 of them are relatively dry airflows with little effect on pollutant removal, favor the
383 accumulation of pollutants near the southern Himalayas, and carry the pollutants to the TP (e.g.,
384 Dumka et al., 2010; Kang et al., 2016; Cong et al., 2015a).

385 The AOD retrieved at two AERONET sites over the TP are compared with the two
386 simulations for April 1-20, 2016 (Fig. 7). The AOD at the QOMS_CAS site near the northern
387 Himalayas is higher than that at the NAM_CO site inside of the TP. Both simulations can
388 capture this gradient. The simulation with complex topography produces higher AOD than
389 does the one with smooth topography at both sites. The modeling biases (normalized mean bias,
390 NMB) reduce from -46% (smooth topography) to 9% (complex topography) at the
391 QOMS_CAS site and from -26% (smooth topography) to -10% (complex topography) at the
392 NAM_CO site. Although the correlation coefficient between the simulations and observation
393 increases from 0.37 (smooth topography) to 0.53 (complex topography) at the QOMS_CAS
394 site, it is similar (~ 0.2) between the two simulations at the NAM_CO site. The correlation
395 coefficient is higher at the QOMS_CAS site near the source region than the NAM_CO site
396 farther away, which may indicate the model processes affecting the transport over the TP still
397 need examination with more observations. The NAM_CO site over the eastern TP may also be
398 affected by other sources that are not counted in this study. The modeling of temporal variations
399 of pollutants over the TP deserves further investigation with more observations.

400 There is one in-situ observational station (QOMS) near the Mt. Everest (black dot shown
401 in Fig. 1) to collect the near-surface BC concentration. The observed near-surface BC
402 concentration at this station is compared with the corresponding simulations for this period as
403 shown in Figure 8. Without local emission source, the near-surface BC concentration at QOMS
404 is primarily contributed by the transport. The temporal variation of observed near-surface BC

405 concentration correlates highly with the biomass burning emissions as shown in Fig. 4, with
406 the peak value on April 11 reaching $\sim 3 \text{ ug/m}^3$. One sensitivity experiment without biomass
407 burning emissions shows that the simulated BC concentration at QOMS will be significantly
408 reduced without the peak (not shown), which further proves that the BC concentration over the
409 northern Himalayas can be largely influenced by the pollution episode near the southern
410 Himalayas. It is noteworthy that both simulations can reproduce the episode in time and
411 magnitude, and the difference at this station is small. The spatial distribution of difference in
412 near-surface BC concentration between the two simulations (Fig. S2) is more heterogeneous
413 than that of column BC mass (Fig. 5), reflecting the impact of topography on near-surface
414 transport (see the discussion in Section 3.2).

415

416 **3.2 Transport flux into the TP**

417 To further understand the difference in BC near-surface concentration and column mass
418 loading over the TP between the two simulations with different topography, Figure 9 shows
419 the longitude-height cross section of BC transport flux along the cross line (shown as the black
420 dash line in Fig. 3) from the two simulations at local time (LT) 03:00 and 15:00 averaged for
421 April 1-20 to represent nighttime and daytime transport, respectively. The PBL height along
422 the cross line is also shown as the black dash line. The transport flux is calculated by projecting
423 the wind field perpendicularly to the cross line and then multiplying the BC mass concentration
424 along the cross line. More specifically, the transport flux is calculated as following:

$$425 \quad \text{TF} = C * (u * \sin \alpha + v * \sin \beta) \quad (1)$$

426 Where α is the angle between east-west wind component and the cross line, β is the angle
427 between south-north wind component and the cross line, and C is the BC mass concentration
428 at the grid along the cross line. The flux is estimated at each model level. Positive values
429 represent the transport towards the TP, while negative values represent the transport away from
430 the TP. It is evident that BC is imported into the TP during the day and night on the west of
431 $\sim 85^\circ\text{E}$, although the transport flux is much larger during the daytime than nighttime. On the
432 east of $\sim 85^\circ\text{E}$, BC is imported into the TP during the day but exported slightly from the TP
433 during the night. The difference of transport flux between the western and eastern Himalayas
434 is primarily due to the influence of large-scale westerly that is weak over the eastern Himalayas
435 (Fig. 5). The transport across the western Himalayas is controlled by the large-scale westerly,
436 while local southerly dominates the transport across the eastern Himalayas and also influences
437 the transport across the central Himalayas (Fig. S3 in the supporting material). The stronger

438 diurnal variation of local southerly (towards the TP in the daytime to away from the TP in the
439 nighttime) than that of westerly near the surface (Fig. S3) leads to the large difference in diurnal
440 variation of transport between the western and eastern Himalayas. The strong transport is
441 primarily within the PBL during the daytime, and the deeper PBL during the daytime allows
442 BC over the source region mixed to higher altitude, which also leads to stronger import
443 transport during the day than the night. The relatively small difference in simulated PBL
444 heights and structure between the two experiments can be due to their different surface heating
445 resulted from different topography complexity (e.g., Wagner et al., 2014).

446 The difference between the simulations with two different topography is evident. The
447 mountain ridges are much higher and valleys are much deeper with the complex topography
448 than with the smooth topography. The simulation with smooth topography produces
449 overwhelming crossing-Himalayas transport towards the TP within the PBL, in particular
450 during the daytime. Although, in the simulation with complex topography, the mountain ridges
451 resolved weaken the crossing-Himalayas transport compared to the simulation with smooth
452 topography, the overall positive values near the surface indicate that the transport can overcome
453 most mountain ridges along the Himalayas. The transport fluxes near the surface from the
454 simulation with complex topography become close-to-zero only at a few mountain ridges that
455 are 6.5 km or higher. To better demonstrate the transport pathway across mountain ridges, one
456 cross-section across the mountain ridge as shown as one black solid line in Fig. 3 is taken as
457 one example. Figure 10 shows the latitude-height cross section of BC mass concentration and
458 transport flux across one mountain ridge from the simulations with complex and smooth
459 topography at local time (LT) 03:00 and 15:00 averaged for April 1-20, 2016. Near the southern
460 part of mountain, the elevated concentration of BC mass accumulates and can mix up reaching
461 as high as 5 km with the much stronger transport during the daytime. It is obvious that the
462 mountain ridge in the simulation with smooth topography is quite low. With the high mountain
463 ridge resolved by the complex topography, the simulated BC transport flux can still cross the
464 mountain. Analysis of transport flux across a few more mountain ridges indicates similar
465 results (not shown). The results above indicate that the transport of pollutants can cross a
466 majority of mountain ridges of Himalayas, which is consistent with the observation-based
467 estimate by Gong et al. (2019) that also found pollutants could overcome the blocking effect
468 of mountain ridges of Himalayas as a transport pathway. On the other hand, the resolved deeper
469 valleys in the simulation with complex topography enhance the transport flux compared to the
470 one with the smooth topography. Similarly, Figure 11 shows one example of latitude-height
471 cross section of BC mass concentration and transport flux across one valley from the

472 simulations with complex and smooth topography at local time (LT) 03:00 and 15:00 averaged
473 for April 1-20, 2016. The transport is much stronger and deeper along the valley from the
474 simulation with complex topography than the one with smooth topography. Again, analysis of
475 transport flux across a few more valleys does not show different results (not shown).

476 In order to further demonstrate the overall inflow flux across the Himalayas, the vertically
477 integrated BC mass flux along the longitudinal cross section (as shown in Fig. 9) from the
478 simulations with different topography is shown in Figure 12. The terrain heights from the two
479 simulations along the cross section are also shown as black lines. The total mass flux is
480 calculated by integrating the right-hand term of equation (1) as following:

$$481 \quad \text{ITF} = \int_{z=z_{sc}}^{z=z_{top}} \delta z * C * (u * \sin \alpha + v * \sin \beta) \quad (2)$$

482 Where δz is the thickness of each vertical model level. Similarly, positive values represent
483 the transport towards the TP, while negative values represent the transport away from the TP.
484 More evidently, the positive BC inflows towards the TP occur not only through the valleys but
485 also across the mountain ridges with both topography. The negative values only exist to the
486 east of 88°E. With complex topography, higher mountain ridges can reduce the transport flux
487 to some extent compared to the smooth topography. The complex topography results in
488 significantly larger BC inflow towards the TP compared to the smooth topography, particularly
489 corresponding to the deep valleys, such as the Karnali River Valley around 82°E and the Kali
490 Gandaki Valley around 84°E.

491 One reason for the enhanced transport across the Himalayas with the complex topography
492 is the resolved deeper valleys that lead to the increased valley wind. The wind across some
493 valleys can be significantly larger with the complex topography than the smooth one (Fig. S3).
494 The enhanced valley wind across the Himalayas has also been found by previous studies with
495 observations and numerical simulations (e.g., Egger et al., 2000; Zängl et al., 2001; Carrera et
496 al., 2009; Karki et al., 2017; Lin et al., 2018). However, it is noteworthy that previous studies
497 have found that the orographic drag (including gravity wave drag and turbulence orographic
498 form drag) over the region with complex topography, such as the Himalayas and other
499 mountainous areas, would weaken the overall near-surface wind speed (e.g., Beljaars et al.,
500 2004; Horvath et al., 2012; Jiménez and Dudhia, 2012; Zhou et al., 2017, 2018; Lin et al., 2018;
501 Wang et al, 2020). Therefore, the near-surface wind speed is also examined. The complex
502 topography does lead to the overall reduction of near-surface wind speed over the Himalayas
503 area (Fig. S4 in the supporting material), which is consistent with previous studies. However,
504 it is interesting to note that the near-surface southerly wind during the daytime of the simulation

505 period is overall increased over the Himalayas area with the complex topography (Fig. 13),
506 which indicates that the transport towards the TP is strengthened with the complex topography
507 in the daytime, particularly over the central and eastern Himalayas where the BC mass loading
508 is higher (Fig. 5). During the night, the meridional wind is dominated by northerly over the
509 Himalayas region in the simulation with the smooth topography. The complex topography
510 weakens the transport away from the TP or change the wind direction from northerly to
511 southerly over some areas of Himalayas. Both effects enhance the overall transport efficiency
512 across the Himalayas towards the TP. Therefore, although the complex topography weakens
513 the overall near-surface wind speed around the Himalayas, it induces more realistic small-scale
514 mountain-valley circulation that favors the BC transport across the Himalayas towards TP
515 during the study period. Another effect of resolving valleys is that the volume of relatively-
516 high-concentration BC could be higher with deeper valleys (Fig. S5 in the support material),
517 which can also result in stronger transport towards the TP even if the wind condition is similar.
518 For example, the altitude (above the ground) below which the BC mass concentration is larger
519 than 0.3 ug/m^3 is much higher along the valleys with the complex topography than with the
520 smooth topography (Fig. S6 in the support material). The correlation coefficient between the
521 difference of terrain heights of valleys and of volumes of relatively-high-concentration BC can
522 reach -0.76, indicating that the lower the valleys are, the higher the volumes of BC mass can
523 be transported across the Himalayas. The combined influence of these factors results in
524 significantly enhanced BC transport towards the TP with the complex topography (Fig. 12),
525 which can also be demonstrated by the distributions of wind and BC mass concentration along
526 the longitudinal cross section (Fig. S7a, b in the support material).

527 The enhanced transport across the Himalayas turns out that the overall BC inflow with the
528 complex topography is much stronger than that with the smooth topography. Figure 14 shows
529 the accumulated integrated total transport flux of BC across the Himalayas estimated from the
530 simulations with complex and smooth topography for April 1-20, 2016. The accumulated
531 import flux of BC increases during the period in both experiments, and the difference between
532 the two experiments gradually increases with the time. At the end of period, the simulation
533 with complex topography estimates a total import flux of BC of $\sim 1.5 \times 10^4$ Ton that is $\sim 50\%$
534 higher than $\sim 1.0 \times 10^4$ Ton estimated based on the simulation with smooth topography. The
535 sensitivity analysis by moving the cross line (cross-section of the analysis in Fig. 9, 12, 14)
536 towards or away from the TP within a certain distance and re-calculating the flux indicates that
537 the impacts of topography on the simulated results do not change significantly.

538 All the analysis above focuses on investigating the BC transport flux across the Himalayas.
539 Although the inflow can reflect the impact of transport on the BC mass over the TP to some
540 extent, the change of BC mass concentration is eventually determined by the convergence of
541 transport. Therefore, the contribution of each model process (transport, dry-deposition,
542 emission, PBL mixing, and wet deposition) to the increase of BC column mass averaged over
543 the TP (with elevation > 4 km) during this episode is analyzed for both simulations following
544 the methodology introduced by Du et al. (2020). The results show that the two main processes
545 affecting the BC column mass over the TP during the period are transport and dry deposition.
546 The transport is the dominant process that increases the BC column mass over the TP, while
547 the dry deposition reduces it. The contribution of transport to the increase of BC column mass
548 over the TP during the episode from the simulation with complex topography is significantly
549 larger than that with the smooth topography, which is consistent with the results shown by
550 analyzing the transport flux across the Himalayas. Although the impacts of PBL mixing and
551 wet deposition on the BC column mass over the TP are also different between the simulations
552 with different topography, their impacts are much smaller than those of transport and dry
553 deposition during the study period.

554

555 **3.3 Radiative forcing of BC over the TP**

556 The BC transported over the TP could significantly influence the regional climate and
557 water resources over Asia through heating the atmosphere and accelerating the melting of snow
558 and glacier (e.g., Qian et al., 2011, 2015; Lau et al., 2017). Therefore, the impact of the complex
559 topography on estimating the BC radiative heating profile in the atmosphere and radiative
560 forcing in surface snow deserves investigation. Figure 15 shows the vertical profiles of BC
561 induced radiative heating rate in the atmosphere averaged over the TP (with elevation > 4 km)
562 within the inner domain shown in Fig.1 for April 1-20, 2016 from the simulations with complex
563 and smooth topography. Both simulations generate higher BC heating rate near the surface and
564 the rate gradually decreases with altitude, which is consistent with the vertical profiles of BC
565 mass concentration averaged over the TP (Fig. S8 in the supporting material). The BC heating
566 rate over the TP from the simulation with complex topography is ~0.17 K/day near the surface
567 and reduces to ~0.08 K/day at 8 km, which is ~50% and ~30%, respectively, higher than that
568 from the simulation with smooth topography at the corresponding altitudes. The higher BC
569 heating rate over the TP estimated by the simulation with complex topography is consistent
570 with its higher BC column mass (Fig. 5) and concentration profile (Fig. S8).

571 The BC radiative forcing in surface snow is controlled by both the distributions of BC
572 mass concentration and snow coverage (e.g., Zhao et al., 2014). Figure 16 shows the spatial
573 distributions of snow water equivalent (SWE) averaged for April 1-20, 2016 from the
574 simulations with two topography. The difference between the two is also shown. It shows that
575 the simulation with complex topography generates more areas with higher SWE compared to
576 that with the smooth topography over the TP. Along the Himalayas, the simulated SWE is
577 higher over the mountain ridges with the complex topography, particularly for the East
578 Himalayas, while the smooth topography leads to broader snow coverage over the West
579 Himalayas. The difference in SWE between the two simulations is highly correlated with their
580 difference in precipitation (Fig. S9 in the supporting material). Along the Himalayas, the
581 simulated precipitation with the complex topography is larger than that with the smooth
582 topography at the mountain ridges and smaller at the valleys. Over the TP, the overall
583 precipitation is larger with the complex topography than that with the smooth topography (Fig.
584 S9). Previous studies have found that the topography could significantly affect the precipitation
585 over the Himalayas region (e.g., Bookhagen and Burbank, 2010; Wulf et al., 2016; Cannon et
586 al., 2017; Karki et al., 2017).

587 Figure 17 shows the spatial distributions of BC radiative forcing in the surface snow over
588 the TP averaged for April 1-20, 2016 from the simulations with two topography, and the
589 difference between the two is also shown. The BC radiative forcing in surface snow is largely
590 coincident with the spatial distributions of SWE as shown in Fig. 16, mainly due to the
591 heterogeneous distributions of snow cover over the TP. The BC radiative forcing in surface
592 snow over the TP from the simulation with complex topography reaches 5 W/m^2 where the
593 snow exists, larger than that with the smooth topography. Along the Himalayas, the simulation
594 with complex topography produces higher BC snow forcing over the mountain ridges,
595 particularly over the eastern Himalayas, while the one with the smooth topography simulates
596 higher BC snow forcing over most areas of western Himalayas due to its broader snow
597 coverage there. Overall, the complex topography leads to higher BC forcing in snow over the
598 TP and the eastern Himalayas and lower BC forcing in snow over the western Himalayas, and
599 therefore results in the different distribution of BC forcing in snow over the TP and Himalayas,
600 compared to that with the smooth topography.

601
602
603

604 **4. Summary**

605 In this study, the model experiments with different topography are conducted to illustrate
606 the impacts of complexity of topography of Himalayas on BC transport from South Asia to the
607 TP. The observed pollution episode at the QOMS station besides the Mt. Everest during the
608 pre-monsoon season is simulated. The observed near-surface BC concentration shows a peak
609 of $\sim 3 \text{ ug/m}^3$ much larger than the background value of $< 0.4 \text{ ug/m}^3$ over the TP. The observed
610 temporal variation of near-surface BC concentrations correlates highly with that of biomass
611 burning emissions near the southern Himalayas, indicating the significant impacts of biomass
612 burning on the pollutants over the TP. The simulations can reproduce the episode in time and
613 magnitude, and are used to investigate the BC transport mechanisms and the impacts of
614 topography.

615 The high BC mass loading during the simulation period accumulates near the southern
616 Himalayas driven by the large-scale westerly and small-scale southerly circulations, which is
617 also observed by satellites. The modeling results demonstrate that the circulations favor the
618 accumulation of pollutants near the Himalayas, particularly over the central and eastern parts,
619 and can carry the pollutants to the TP during the study period, which is consistent with previous
620 modeling studies (e.g., Kopacz et al., 2011). It is noteworthy that the BC accumulated near the
621 southern Himalayas can be transported across the Himalayas overcoming a majority of
622 mountain ridges, which is consistent with the observation-based estimate by Gong et al. (2019)
623 that also found pollutants could overcome the blocking effect of the mountain ridges of
624 Himalayas. However, the transport through the valleys is found much stronger and more
625 efficient than across the mountain ridges and the enhancement effect cannot be ignored. The
626 complex topography results in 50% higher overall transport flux across the Himalayas during
627 the simulation period than that with the smooth topography, primarily due to the strengthened
628 efficiency of near-surface meridional transport towards the TP, enhanced wind speed at some
629 valleys, and deeper valley channels associated with larger BC mass volume that can be
630 transported into the TP, although the overall wind speed is weakened due to the orographic
631 drags with the complex topography. This turns out that the simulation with complex
632 topography produces 30-50% higher BC radiative heating rate in the atmosphere up to 10 km
633 averaged over the TP than does the simulation with smooth topography.

634 For the BC radiative forcing in surface snow, the simulation with complex topography
635 produces stronger forcing over the TP than that with the smooth one. The complex topography
636 makes the distribution of BC forcing in surface snow quite different from the simulation with

637 smooth topography, partly due to its different distribution of surface snow. The simulated BC
638 radiative forcing in snow is distributed more heterogeneously than those in previous studies
639 using global models at relatively coarse resolutions (e.g., Qian et al., 2011). He et al. (2014)
640 used a global chemical transport model to simulate the BC forcing in snow at the horizontal
641 resolution of $\sim 0.2^\circ$ and obtained the similar distribution as the simulation with smooth
642 topography in this study with the high values over the western Himalayas. However, their
643 simulated values near the Himalayas are higher than the simulated results of this study, which
644 may be due to their estimation are averaged for November-April.

645 This study highlights the importance of resolving complex topography of the Himalayas
646 in modeling the aerosol transport across the Himalayas and radiative impact over the TP.
647 Although this study focuses on the impacts of topography on the simulated results, the
648 additional analysis (Fig. S10-12 in the supporting material) of the outer domain simulation at
649 20-km resolution and the inner domain simulation at 4 km with different topography indicates
650 that the resolution-dependent difference between 20 km and 4 km is largely contributed by
651 their different representations of topography over the Himalayas region, consistent with
652 previous studies (e.g., Karki et al., 2017; Lin et al., 2018). Climate models at coarser horizontal
653 resolutions than 20 km and thus with relatively smooth topography may underestimate the
654 aerosol transport from South Asia to the TP during the pre-monsoon season and represent
655 inappropriately the aerosol radiative forcing in the atmosphere and surface snow over the TP.

656

657 **5. Discussion**

658 Previous studies also found the induced change of circulation and transport due to the
659 complex topography at convection-permitting scales with the focus on the meteorological
660 fields over the Himalayas and TP regions (e.g., Karki et al., 2017; Zhou et al., 2017, 2018; Lin
661 et al., 2018; Wang et al., 2020). Most of them either conducted the sub-10 km simulations
662 covering a relatively smaller region (e.g., 101×96 grids at 5 km in Karki et al., 2017; 181×121
663 grids at 2 km in Lin et al., 2018; $\sim 330 \times 230$ grids at 3 km in Wang et al., 2020) compared to
664 this study (400×300 grids at 4 km) or conducted the simulations covering the entire Himalayas
665 but at the resolutions above 10 km and with the sub-grid orographic drag parameterization to
666 consider the impact of complex topography. Although some of previous studies also showed
667 that the resolved complex topography yielded more realistic small-scale mountain-valley
668 circulations and enhanced valley winds over the Himalayas region compared to the smoother

669 topography, the overall moisture transport across the Himalayas towards the TP was weaker
670 with the complex topography due to the orographic drags.

671 The difference between previous studies and this study can be due to several factors. First,
672 previous studies focused on moisture instead of air pollutants. The spatial (horizontal and
673 vertical) distributions between air pollutants and moisture are different and may contribute to
674 the different impacts of topography on the overall transport flux across the Himalayas.
675 However, the analysis of the moisture from the simulations in this study shows the increase of
676 moisture transport (not shown) and hence the increase of precipitation over the TP with the
677 complex topography (Fig. S9). Second, most of previous studies focused on monsoon season
678 instead of pre-monsoon season. Therefore, the meteorological simulations for monsoon season
679 (June-July-August) at different resolutions are also conducted in this study. The results show
680 that the moisture transport and precipitation are reduced at the higher resolution with complex
681 topography and the meridional wind is overall weakened particularly over the central and
682 eastern Himalayas and TP (not shown), which is consistent with previous studies. This may
683 indicate that the different large-scale circulations between the two seasons (much stronger
684 southerly during the monsoon season) may also lead to different impacts of complex
685 topography on meridional winds and hence cross-Himalayas transport.

686 Since this study only demonstrates the potential impacts for a relatively short period, a
687 longer-term study should be conducted to examine the impacts of topography on aerosol
688 climatic effect over the TP in both pre-monsoon and monsoon seasons. In addition, the active
689 convection during the monsoon season may also play an important role on pollutant transport
690 across the Himalayas, which deserves further investigation. Furthermore, aerosol impact on
691 cloud and precipitation, particularly during the monsoon season, and thus on the latent heat in
692 the atmosphere and the associated responses may also depend on the complex topography.
693 Previous studies based on observations found that the rain frequency and intensity reached the
694 highest and the cloud thickness reached the deepest at the foothill of Himalayas and decreased
695 as the elevation increased up to the TP (e.g., Chen et al., 2017; Fu et al., 2018; Zhang et al.,
696 2018), which was explained by Fu et al. (2018) due to the blocking of the air flow by the steep
697 slope of southern Himalayas. However, the large amount of transported aerosol along the slope
698 from the foothill up to the TP may also play a role. These potential impacts of aerosols on
699 regional hydro-climate around the TP and over Asia using high-resolution model that can
700 resolve the complex topography of Himalayas and TP deserve further investigation.

701

702 **Data availability**

703 The released version of WRF-Chem can be downloaded from
704 http://www2.mmm.ucar.edu/wrf/users/download/get_source.html. The updated USTC
705 version of WRF-Chem can be downloaded from <http://aemol.ustc.edu.cn/product/list/> or
706 contact chunzhao@ustc.edu.cn. Also, the code modifications will be incorporated the release
707 version of WRF-Chem in future.

708

709 **Author contributions**

710 Meixin Zhang and Chun Zhao designed the experiments, conducted and analyzed the
711 simulations. All authors contributed to the discussion and final version of the paper.

712

713 **Acknowledgements**

714 This research was supported by the National Key Research and Development Program of
715 China (2016YFA0602001), the National Natural Science Foundation of China NSFC (Grant
716 No. 91837310), the second Tibetan Plateau Scientific Expedition and Research Program (STEP)
717 (2019QZKK0605), and the Fundamental Research Funds for the Central Universities. The
718 study used computing resources from the High-Performance Computing Center of University
719 of Science and Technology of China (USTC) and the TH-2 of National Supercomputer Center
720 in Guangzhou (NSCC-GZ).

721

722 **Reference**

- 727 Bansal, O., Singh, A., and Singh, D.: Characteristics of Black Carbon aerosols over Patiala
728 Northwestern part of the IGP: Source apportionment using cluster and CWT analysis,
729 Atmospheric Pollution Research, 10, 244–256, doi:10.1016/j.apr.2018.08.001, 2019.
- 730 Barnard, J. C., Fast, J. D., Paredes-Miranda, G., Arnott, W. P., and Laskin, A.: Technical Note:
731 Evaluation of the WRF-Chem "Aerosol Chemical to Aerosol Optical Properties" Module
732 using data from the MILAGRO campaign, Atmos. Chem. Phys., 10, 7325–7340,
733 doi:10.5194/acp-10-7325-2010, 2010.
- 734 Beljaars, A. C., Brown, A. R., and Wood, N.: A new parametrization of turbulent orographic
735 form drag, QJ Roy. Meteorol. Soc., 130, 1327–1347, doi: 10.1256/qj.03.73, 2004.
- 736 Barnett, T. P., Adam, J. C., and Lettenmaier, D. P.: Potential impacts of a warming climate on
737 water availability in snow-dominated regions, Nature, 438, 303–309,
738 doi:10.1038/nature04141, 2005.
- 739 Binkowski, F. S. and Shankar, U.: The Regional Particulate Matter Model: 1. Model
740 description and preliminary results, J. Geophys. Res., 100, 26191, doi:10.1029/95JD02093,
741 1995.
- 742 Bookhagen, B. and Burbank, D. W.: Toward a complete Himalayan hydrological budget:
743 Spatiotemporal distribution of snowmelt and rainfall and their impact on river discharge, J.
744 Geophys. Res., 115, 39, doi:10.1029/2009JF001426, 2010.
- 745 Boos, W. R. and Kuang, Z.: Sensitivity of the South Asian monsoon to elevated and non-
746 elevated heating, Scientific reports, 3, 1192, doi:10.1038/srep01192, 2013.
- 747 Cannon, F., Carvalho, L. M. V., Jones, C., Norris, J., Bookhagen, B., and Kiladis, G. N.: Effects
748 of topographic smoothing on the simulation of winter precipitation in High Mountain Asia,
749 J. Geophys. Res. Atmos., 122, 1456–1474, doi:10.1002/2016JD026038, 2017.
- 750 Cao, J., Tie, X., Xu, B., Zhao, Z., Zhu, C., Li, G., and Liu, S.: Measuring and modeling black
751 carbon (BC) contamination in the SE Tibetan Plateau, Journal of Atmospheric Chemistry,
752 67, 45–60, doi:10.1007/s10874-011-9202-5, 2010.
- 753 Carrera, M. L., Gyakum, J. R., and Lin, C. A.: Observational Study of Wind Channeling within
754 the St. Lawrence River Valley, J. Appl. Meteorol. Clim., 48, 2341–2361,
755 doi:10.1175/2009JAMC2061.1, 2009.
- 756 Chapman, E. G., Gustafson, W. I., Easter, R. C., Barnard, J. C., Ghan, S. J., Pekour, M. S., and
757 Fast, J. D.: Coupling aerosol-cloud-radiative processes in the WRF-Chem model:

758 Investigating the radiative impact of elevated point sources, *Atmos. Chem. Phys.*, 9, 945–
759 964, doi:10.5194/acp-9-945-2009, 2009.

760 Chen, J. and Bordoni, S.: Orographic Effects of the Tibetan Plateau on the East Asian Summer
761 Monsoon: An Energetic Perspective, *J. Climate*, 27, 3052–3072, doi:10.1175/JCLI-D-13-
762 00479.1, 2014.

763 Chen, X., Kang, S., Cong, Z., Yang, J., and Ma, Y.: Concentration, temporal variation, and
764 sources of black carbon in the Mt. Everest region retrieved by real-time observation and
765 simulation, *Atmos. Chem. Phys.*, 18, 12859–12875, doi:10.5194/acp-18-12859-2018, 2018.

766 Chen, Y., Fu, Y., Xian, T., and Pan, X.: Characteristics of cloud cluster over the steep southern
767 slopes of the Himalayas observed by CloudSat, *Int. J. Climatol.*, 37, 4043–4052,
768 doi:10.1002/joc.4992, 2017.

769 Cong, Z., Kang, S., and Qin, D.: Seasonal features of aerosol particles recorded in snow from
770 Mt. Qomolangma (Everest) and their environmental implications, *Journal of environmental
771 sciences (China)*, 21, 914–919, doi:10.1016/S1001-0742(08)62361-X, 2009.

772 Cong, Z., Kang, S., Kawamura, K., Liu, B., Wan, X., Wang, Z., Gao, S., and Fu, P.:
773 Carbonaceous aerosols on the south edge of the Tibetan Plateau: concentrations, seasonality
774 and sources, *Atmos. Chem. Phys.*, 15, 1573–1584, doi:10.5194/acp-15-1573-2015, 2015a.

775 Cong, Z., Kawamura, K., Kang, S., and Fu, P.: Penetration of biomass-burning emissions from
776 South Asia through the Himalayas: new insights from atmospheric organic acids, *Scientific
777 reports*, 5, 9580, doi:10.1038/srep09580, 2015b.

778 Dentener, F., Kinne, S., Bond, T., Boucher, O., Cofala, J., Generoso, S., Ginoux, P., Gong, S.,
779 Hoelzemann, J. J., Ito, A., Marelli, L., Penner, J. E., Putaud, J. P., Textor, C., Schulz, M.,
780 van der Werf, G. R., and Wilson, J.: Emissions of primary aerosol and precursor gases in the
781 years 2000 and 1750, prescribed data-sets for AeroCom, *Atmos. Chem. Phys.*, 6, 4321–4344,
782 doi:10.5194/acp-6-4321-2006, 2006.

783 Ding, Y., Sun, Y., Wang, Z., Zhu, Y., and Song, Y.: Inter-decadal variation of the summer
784 precipitation in China and its association with decreasing Asian summer monsoon Part II:
785 Possible causes, *Int. J. Climatol.*, 29, 1926–1944, doi:10.1002/joc.1759, 2009.

786 Du, Q., Zhao, C., Zhang, M., Dong, X., Chen, Y., Liu, Z., Hu, Z., Zhang, Q., Li, Y., Yuan, R.,
787 , and Miao, S.: Modelling diurnal variation of surface PM_{2.5} concentration over East China
788 with WRF-Chem: Impacts from boundary layer mixing and anthropogenic
789 emission, *Atmos. Chem. Phys. Discuss.*, [https://doi.org/10.5194/acp-2019-](https://doi.org/10.5194/acp-2019-739)
790 739, in review, 2020.

791 Duan, A. M. and Wu, G. X.: Role of the Tibetan Plateau thermal forcing in the summer climate
792 patterns over subtropical Asia, *Climate Dynamics*, 24, 793–807, doi:10.1007/s00382-004-
793 0488-8, 2005.

794 Dubovik, O. and King, M. D.: A flexible inversion algorithm for retrieval of aerosol optical
795 properties from Sun and sky radiance measurements, *J. Geophys. Res.*, 105, 20673–20696,
796 doi:10.1029/2000JD900282, 2000.

797 Dubovik, O., Holben, B., Eck, T. F., Smirnov, A., Kaufman, Y. J., King, M. D., Tanré, D., and
798 Slutsker, I.: Variability of Absorption and Optical Properties of Key Aerosol Types
799 Observed in Worldwide Locations, *J. Atmos. Sci.*, 59, 590–608, doi:10.1175/1520-
800 0469(2002)059<0590:VOAAOP>2.0.CO;2, 2002.

801 Dumka, U. C., Moorthy, K. K., Kumar, R., Hegde, P., Sagar, R., Pant, P., Singh, N., and Babu,
802 S. S.: Characteristics of aerosol black carbon mass concentration over a high altitude location
803 in the Central Himalayas from multi-year measurements, *Atmospheric Research*, 96, 510–
804 521, doi:10.1016/j.atmosres.2009.12.010, 2010.

805 Easter, R. C., Ghan, S. J., Zhang, Y., Saylor, R. D., Chapman, E. G., Laulainen, N. S., Abdul-
806 Razzak, H., Leung, L. R., Bian, X., and Zaveri, R. A.: MIRAGE: Model Description and
807 Evaluation of Aerosols and Trace Gases, *J. Geophys. Res.*, 109, D20210,
808 doi:10.1029/2004JD004571, 2004.

809 Egger, J., Bajracharya, S., Egger, U., Heinrich, R., Reuder, J., Shakya, P., Wendt, H., and Wirth,
810 V.: Diurnal winds in the Himalayan Kali Gandaki Valley. Part I: Observations, *Mon.*
811 *Weather Rev.*, 128, 1106–1122, 2000.

812 Engling, G. and Gelencser, A.: Atmospheric Brown Clouds: From Local Air Pollution to
813 Climate Change, *Elements*, 6, 223–228, doi:10.2113/gselements.6.4.223, 2010.

814 Fan, J., Rosenfeld, D., Yang, Y., Zhao, C., Leung, L. R., and Li, Z.: Substantial contribution
815 of anthropogenic air pollution to catastrophic floods in Southwest China, *Geophys. Res. Lett.*,
816 42, 6066–6075, doi:10.1002/2015GL064479, 2015.

817 Fast, J. D., Gustafson Jr, W. I., Easter, R. C., Zaveri, R. A., Barnard, J. C., Chapman, E. G.,
818 Grell, G. A., and Peckham, S. E.: Evolution of ozone, particulates, and aerosol direct
819 radiative forcing in the vicinity of Houston using a fully coupled meteorology-chemistry-
820 aerosol model, *J. Geophys. Res.*, 111, D21305, doi:10.1029/2005JD006721, 2006.

821 Feng, Y., Kotamarthi, V. R., Coulter, R., Zhao, C., and Cadeddu, M.: Radiative and
822 thermodynamic responses to aerosol extinction profiles during the pre-monsoon month over
823 South Asia, *Atmos. Chem. Phys.*, 16, 247–264, doi:10.5194/acp-16-247-2016, 2016.

824 Flanner, M. G. and Zender, C. S.: Snowpack radiative heating: Influence on Tibetan Plateau
825 climate, *Geophys. Res. Lett.*, 32, L06501, doi:10.1029/2004GL022076, 2005.

826 Fu, Y., Pan, X., Xian, T., Liu, G., Zhong, L., Liu, Q., Li, R., Wang, Y., and Ma, M.:
827 Precipitation characteristics over the steep slope of the Himalayas in rainy season observed
828 by TRMM PR and VIRS, *Climate dynamics*, 51, 1971-1989, doi: 10.1007/s00382-017-
829 3992-3, 2018.

830 Gao, Y., Zhao, C., Liu, X., Zhang, M., and Leung, L. R.: WRF-Chem simulations of aerosols
831 and anthropogenic aerosol radiative forcing in East Asia, *Atmospheric Environment*, 92,
832 250–266, doi:10.1016/j.atmosenv.2014.04.038, 2014.

833 Ginoux, P., Chin, M., Tegen, I., Prospero, J. M., Holben, B., Dubovik, O., and Lin, S.-J.:
834 Sources and distributions of dust aerosols simulated with the GOCART model, *J. Geophys.*
835 *Res.*, 106, 20255–20273, doi:10.1029/2000JD000053, 2001.

836 Gong, P., Wang, X., Pokhrel, B., Wang, H., Liu, X., Liu, X., and Wania, F.: Trans-Himalayan
837 Transport of Organochlorine Compounds: Three-Year Observations and Model-Based Flux
838 Estimation, *Environ. Sci. Technol.*, 53, 6773–6783, doi:10.1021/acs.est.9b01223, 2019.

839 Gong, S. L.: A parameterization of sea-salt aerosol source function for sub- and super-micron
840 particles, *Global Biogeochem. Cycles*, 17, n/a-n/a, doi:10.1029/2003GB002079, 2003.

841 Grell, G. A., Peckham, S. E., Schmitz, R., McKeen, S. A., Frost, G., Skamarock, W. C., and
842 Eder, B.: Fully coupled “online” chemistry within the WRF model, *Atmospheric*
843 *Environment*, 39, 6957–6975, doi:10.1016/j.atmosenv.2005.04.027, 2005.

844 Gustafson, W. I., E. G. Chapman, S. J. Ghan, R. C. Easter, and J. D. Fast: Impact on modeled
845 cloud characteristics due to simplified treatment of uniform cloud condensation nuclei
846 during NEAQS 2004, *Geophys. Res. Lett.*, 34, L19809, doi:10.1029/2007GL030021, 2007.

847 Hansen, J. and Nazarenko, L.: Soot climate forcing via snow and ice albedos, *Proceedings of*
848 *the National Academy of Sciences*, 101, 423–428, doi:10.1073/pnas.2237157100, 2004.

849 He, C., Li, Q., Liou, K. N., Takano, Y., Gu, Y., Qi, L., Mao, Y., and Leung, L. R.: Black carbon
850 radiative forcing over the Tibetan Plateau, *Geophys. Res. Lett.*, 41, 7806–7813,
851 doi:10.1002/2014GL062191, 2014.

852 He, C., Wang, Z., Zhou, T., and Li, T.: Enhanced Latent Heating over the Tibetan Plateau as a
853 Key to the Enhanced East Asian Summer Monsoon Circulation under a Warming Climate,
854 *J. Climate*, 32, 3373–3388, doi:10.1175/JCLI-D-18-0427.1, 2019.

855 Hess, M., Koepke, P., and Schult, I.: Optical Properties of Aerosols and Clouds: The Software
856 Package OPAC, *Bull. Amer. Meteor. Soc.*, 79, 831–844, doi:10.1175/1520-
857 0477(1998)079<0831:OPOAAC>2.0.CO;2, 1998.

858 Hindman, E. E. and Upadhyay, B. P.: Air pollution transport in the Himalayas of Nepal and
859 Tibet during the 1995–1996 dry season, *Atmospheric Environment*, 36, 727–739,
860 doi:10.1016/S1352-2310(01)00495-2, 2002.

861 Holben, B. N., Eck, T. F., Slutsker, I., Tanré, D., Buis, J. P., Setzer, A., Vermote, E., Reagan,
862 J. A., Kaufman, Y. J., Nakajima, T., Lavenu, F., Jankowiak, I., and Smirnov, A.:
863 AERONET—A Federated Instrument Network and Data Archive for Aerosol
864 Characterization, *Remote Sensing of Environment*, 66, 1–16, doi:10.1016/S0034-
865 4257(98)00031-5, 1998.

866 Holben, B. N., Tanre, D., Smirnov, A., ECK T. F., Slutsker, I., Abuhassan, N., Newcomb, W.,
867 Schafer, J., Chatenet, B., Lavenu, F., Kaufman, Y., Vande Castle, J., Setzer, A., Markham,
868 B., Clark, D., Frouin, R., Halthore, R., Karneli, A., O'Neill, N., Pietras, C., Pinker, R., Voss,
869 K., and Zibordi, G.: An emerging ground-based aerosol climatology: Aerosol optical depth
870 from AERONET, *J. Geophys. Res.*, 106, 12067-12097, doi:10.1029/2001JD900014, 2001.

873 Horvath, K., Koracin, D., Vellore, R., Jiang, J., and Belu, R.: Sub - kilometer dynamical
874 downscaling of near - surface winds in complex terrain using WRF and MM5 mesoscale
875 models, *J. Geophys. Res. Atmos.*, 117, D11111, doi:10.1029/2012JD017432, 2012

876 Hu, Z., Huang, J., Zhao, C., Bi, J., Jin, Q., Qian, Y., Leung, L. R., Feng, T., Chen, S., and Ma,
877 J.: Modeling the contributions of Northern Hemisphere dust sources to dust outflow from
878 East Asia, *Atmospheric Environment*, 202, 234–243, doi:10.1016/j.atmosenv.2019.01.022,
879 2019.

880 Hu, Z., Huang, J., Zhao, C., Jin, Q., Ma, Y., and Yang, B.: Modeling dust sources, transport,
881 and radiative effects at different altitudes over the Tibetan Plateau, *Atmos. Chem. Phys.*
882 *Discuss.*, <https://doi.org/10.5194/acp-2019-431>, in press, 2020.

883 Hu, Z., Zhao, C., Huang, J., Leung, L. R., Qian, Y., Yu, H., Huang, L., and Kalashnikova, O.V.:
884 Trans-pacific transport and evolution of aerosols: Evaluation of quasi global WRF-Chem
885 simulation with multiple observations, *Geosci. Model Dev.*, 9, 1725–1746, doi:10.5194/
886 gmd-9-1725-2016, 2016.

887 Huang, X., Song, Y., Zhao, C., Cai, X., Zhang, H., and Zhu, T.: Direct Radiative Effect by
888 Multicomponent Aerosol over China, *J. Climate*, 28, 3472–3495, doi:10.1175/JCLI-D-14-
889 00365.1, 2015.

890 Iacono, M. J., Mlawer, E. J., Clough, S. A., and Morcrette, J. J.: Impact of an improved
891 longwave radiation model, RRTM, on the energy budget and thermodynamic properties of

892 the NCAR community climate model, CCM3, *J. Geophys. Res.*, 105, 14873–14890,
893 doi:10.1029/2000JD900091, 2000.

894 Immerzeel, W. W., van Beek, L. P. H., and Bierkens, M. F. P.: Climate change will affect the
895 Asian water towers, *Science* (New York, N.Y.), 328, 1382–1385,
896 doi:10.1126/science.1183188, 2010.

897 Jaeglé, L., Quinn, P. K., Bates, T. S., Alexander, B., and Lin, J. T.: Global distribution of sea
898 salt aerosols: new constraints from in situ and remote sensing observations, *Atmos. Chem.*
899 *Phys.*, 11, 3137–3157, doi:10.5194/acp-11-3137-2011, 2011.

900 Janssens-Maenhout, G., Crippa, M., Guizzardi, D., Dentener, F., Muntean, M., Pouliot, G.,
901 Keating, T., Zhang, Q., Kurokawa, J., Wankmüller, R., van der Denier Gon, H., Kuenen, J.
902 J. P., Klimont, Z., Frost, G., Darras, S., Koffi, B., and Li, M.: HTAP_v2.2: a mosaic of
903 regional and global emission grid maps for 2008 and 2010 to study hemispheric transport of
904 air pollution, *Atmos. Chem. Phys.*, 15, 11411–11432, doi:10.5194/acp-15-11411-2015,
905 2015.

906 Ji, Z. M.: Modeling black carbon and its potential radiative effects over the Tibetan Plateau,
907 *Advances in Climate Change Research*, 7, 139–144, doi:10.1016/j.accre.2016.10.002, 2016.

908 Ji, Z., Kang, S., Cong, Z., Zhang, Q., and Yao, T.: Simulation of carbonaceous aerosols over
909 the Third Pole and adjacent regions: distribution, transportation, deposition, and climatic
910 effects, *Clim Dyn*, 45, 2831–2846, doi:10.1007/s00382-015-2509-1, 2015.

911 Jiménez, P. A. and Dudhia, J.: Improving the representation of resolved and unresolved
912 topographic effects on surface wind in the WRF model, *J. Appl. Meteorol. Clim.*, 51, 300-
913 316, doi:10.1175/JAMC-D-11-084.1, 2012.

914 Kain, J. S.: The Kain–Fritsch Convective Parameterization: An Update, *J. Appl. Meteor.*, 43,
915 170–181, doi:10.1175/1520-0450(2004)043<0170:TKCPAU>2.0.CO;2, 2004.

916 Kang, S, Chen P, Li C, Liu B, Cong Z: Atmospheric Aerosol Elements over the Inland Tibetan
917 Plateau: Concentration, Seasonality, and Transport, *Aerosol Air Qual. Res.*, 16, 789–800,
918 doi:10.4209/aaqr.2015.02.0307, 2016.

919 Kang, S., Q. Zhang, Y. Qian, Z. Ji, C. Li, Z. Cong, Y. Zhang, J. Guo, W. Du, J. Huang, Q. You,
920 A. K. Panday, M. Rupakheti, D. Chen, O. Gustafsson, M. H. Thiemens, and D. Qin: Linking
921 atmospheric pollution to cryospheric change in the Third Pole region: current progress and
922 future prospects, *National Science Review*, 6, 796–809, doi:10.1093/nsr/nwz031, 2019.

923 Kant, Y., Shaik, D. S., Mitra, D., Chandola, H. C., Babu, S. S., and Chauhan, P.: Black carbon
924 aerosol quantification over north-west Himalayas: Seasonal heterogeneity, source

925 apportionment and radiative forcing, *Environmental pollution* (Barking, Essex 1987),
926 113446, doi:10.1016/j.envpol.2019.113446, 2019.

927 Karki, R., ul Hasson, S., Gerlitz, L., Schickhoff, U., Scholten, T., and Böhner, J.: Quantifying
928 the added value of convection-permitting climate simulations in complex terrain: a
929 systematic evaluation of WRF over the Himalayas, *Earth Syst. Dynam.*, 8, 507–528,
930 doi:10.5194/esd-8-507-2017, 2017.

931 Kok, J. F.: A scaling theory for the size distribution of emitted dust aerosols suggests climate
932 models underestimate the size of the global dust cycle, *Proceedings of the National Academy
933 of Sciences of the United States of America*, 108, 1016–1021, doi:10.1073/pnas.1014798108,
934 2011.

935 Kopacz, M., Mauzerall, D. L., Wang, J., Leibensperger, E. M., Henze, D. K., and Singh, K.:
936 Origin and radiative forcing of black carbon transported to the Himalayas and Tibetan
937 Plateau, *Atmos. Chem. Phys.*, 11, 2837–2852, doi:10.5194/acp-11-2837-2011, 2011.

938 Kuhlmann, J. and Quaas, J.: How can aerosols affect the Asian summer monsoon? Assessment
939 during three consecutive pre-monsoon seasons from CALIPSO satellite data, *Atmos. Chem.
940 Phys.*, 10, 4673–4688, doi:10.5194/acp-10-4673-2010, 2010.

941 Lau, K. M. and Kim, K. M.: Observational relationships between aerosol and Asian monsoon
942 rainfall, and circulation, *Geophys. Res. Lett.*, 33, D22101, doi: 10.1029/2006GL027546,
943 2006b.

944 Lau, K. M., Kim, M. K., and Kim, K. M.: Asian summer monsoon anomalies induced by
945 aerosol direct forcing: the role of the Tibetan Plateau, *Clim Dyn*, 26, 855–864, doi:
946 10.1007/s00382-006-0114-z, 2006a.

947 Lau, W. K. and Kim, K. M.: Impact of Snow Darkening by Deposition of Light-Absorbing
948 Aerosols on Snow Cover in the Himalayas–Tibetan Plateau and Influence on the Asian
949 Summer Monsoon: A Possible Mechanism for the Blanford Hypothesis, *Atmosphere*, 9, 438,
950 doi:10.3390/atmos9110438, 2018.

951 Lau, W. K. M., Kim, K. M., Shi, J. J., Matsui, T., Chin, M., Tan, Q., Peters-Lidard, C., and
952 Tao, W. K.: Impacts of aerosol–monsoon interaction on rainfall and circulation over
953 Northern India and the Himalaya Foothills, *Clim Dyn*, 49, 1945–1960, doi:10.1007/s00382-
954 016-3430-y, 2017.

955 Lau, W. K. M., Kim, M. K., Kim, K. M., and Lee, W. S.: Enhanced surface warming and
956 accelerated snow melt in the Himalayas and Tibetan Plateau induced by absorbing aerosols,
957 *Environ. Res. Lett.*, 5, 25204, doi:10.1088/1748-9326/5/2/025204, 2010.

958 Lee, W. S., Bhawar, R. L., Kim, M. K., and Sang, J.: Study of aerosol effect on accelerated
959 snow melting over the Tibetan Plateau during boreal spring, *Atmospheric Environment*, 75,
960 113–122, doi:10.1016/j.atmosenv.2013.04.004, 2013.

961 Li, C., Bosch, C., Kang, S., Andersson, A., Chen, P., Zhang, Q., Cong, Z., Chen, B., Qin, D.,
962 and Gustafsson, Ö.: Sources of black carbon to the Himalayan–Tibetan Plateau glaciers, *Nat*
963 *Commun*, 7, 4825, doi:10.1038/ncomms12574, 2016.

964 Li, M., Zhang, Q., Kurokawa, J. i., Woo, J. H., He, K., Lu, Z., Ohara, T., Song, Y., Streets, D.
965 G., Carmichael, G. R., Cheng, Y., Hong, C., Huo, H., Jiang, X., Kang, S., Liu, F., Su, H.,
966 and Zheng, B.: MIX: a mosaic Asian anthropogenic emission inventory under the
967 international collaboration framework of the MICS-Asia and HTAP, *Atmos. Chem. Phys.*,
968 17, 935–963, doi:10.5194/acp-17-935-2017, 2017.

969 Li, R. and Min, Q. L.: Impacts of mineral dust on the vertical structure of precipitation, *J.*
970 *Geophys. Res.*, 115, 1337, doi:10.1029/2009JD011925, 2010.

971 Li, R., Dong, X., Guo, J., Fu, Y., Zhao, C., Wang, Y., and Min, Q.: The implications of dust
972 ice nuclei effect on cloud top temperature in a complex mesoscale convective system, *Sci*
973 *Rep*, 7, 291, doi:10.1038/s41598-017-12681-0, 2017.

974 Li, R., Shao, W., Guo, J., Fu, Y., Wang, Y., Liu, G., Zhou, R., and Li, W.: A Simplified
975 Algorithm to Estimate Latent Heating Rate Using Vertical Rainfall Profiles Over the Tibetan
976 Plateau, *J. Geophys. Res. Atmos.*, 124, 942–963, doi:10.1029/2018JD029297, 2019.

977 Lin, C., Chen, D., Yang, K., and Ou, T.: Impact of model resolution on simulating the water
978 vapor transport through the central Himalayas: implication for models’ wet bias over the
979 Tibetan Plateau, *Clim Dyn*, 51, 3195–3207, doi:10.1007/s00382-018-4074-x, 2018.

980 Liu, P., Tsimpidi, A. P., Hu, Y., Stone, B., Russell, A. G., and Nenes, A.: Differences between
981 downscaling with spectral and grid nudging using WRF, *Atmos. Chem. Phys.*, 12, 3601–
982 3610, doi:10.5194/acp-12-3601-2012, 2012.

983 Liu, Y., Sato, Y., Jia, R., Xie, Y., Huang, J., and Nakajima, T.: Modeling study on the transport
984 of summer dust and anthropogenic aerosols over the Tibetan Plateau, *Atmos. Chem. Phys.*,
985 15, 12581–12594, doi:10.5194/acp-15-12581-2015, 2015.

986 Liu, Z., Ming, Y., Zhao, C., Lau, N. C., Guo, J., Bollasina, M., and Yim, S. H. L.: Contribution
987 of local and remote anthropogenic aerosols to a record-breaking torrential rainfall event in
988 Guangdong Province, China, *Atmos. Chem. Phys.*, 20, 223–241, doi:10.5194/acp-20-223-
989 2020, 2020.

990 Lu, Z., Streets, D. G., Zhang, Q., and Wang, S.: A novel back-trajectory analysis of the origin
 991 of black carbon transported to the Himalayas and Tibetan Plateau during 1996-2010,
 992 *Geophys. Res. Lett.*, 39, n/a-n/a, doi:10.1029/2011GL049903, 2012.

993 Lüthi, Z. L., Škerlak, B., Kim, S. W., Lauer, A., Mues, A., Rupakheti, M., and Kang, S.:
 994 Atmospheric brown clouds reach the Tibetan Plateau by crossing the Himalayas, *Atmos.*
 995 *Chem. Phys.*, 15, 6007–6021, doi:10.5194/acp-15-6007-2015, 2015.

996 Lutz, A. F., Immerzeel, W. W., Shrestha, A. B., and Bierkens, M. F. P.: Consistent increase in
 997 High Asia's runoff due to increasing glacier melt and precipitation, *Nature Clim Change*, 4,
 998 587–592, doi:10.1038/nclimate2237, 2014.

999 Marinoni, A., Cristofanelli, P., Laj, P., Duchi, R., Calzolari, F., Decesari, S., Sellegri, K.,
 1000 Vuillermoz, E., Verza, G. P., and Villani, P.: Aerosol mass and black carbon concentrations,
 1001 a two year record at NCO-P (5079 m, Southern Himalayas), *Atmos. Chem. Phys.*, 10, 8551–
 1002 8562, doi:10.5194/acp-10-8551-2010, 2010.

1003 Menon, S., Koch, D., Beig, G., Sahu, S., Fasullo, J., and Orlikowski, D.: Black carbon aerosols
 1004 and the third polar ice cap, *Atmos. Chem. Phys.*, 10, 4559–4571, doi:10.5194/acp-10-4559-
 1005 2010, 2010.

1006 Ming, J., Xiao, C., Cachier, H., Qin, D., Qin, X., Li, Z., and Pu, J.: Black Carbon (BC) in the
 1007 snow of glaciers in west China and its potential effects on albedos, *Atmospheric Research*,
 1008 92, 114–123, doi:10.1016/j.atmosres.2008.09.007, 2009.

1009 Mlawer, E. J., Taubman, S. J., Brown, P. D., Iacono, M. J., and Clough, S. A.: Radiative
 1010 transfer for inhomogeneous atmospheres: RRTM, a validated correlated-k model for the
 1011 longwave, *J. Geophys. Res.*, 102, 16663–16682, doi:10.1029/97JD00237, 1997.

1012 Morrison, H., Thompson, G., and Tatarskii, V.: Impact of Cloud Microphysics on the
 1013 Development of Trailing Stratiform Precipitation in a Simulated Squall Line: Comparison
 1014 of One- and Two-Moment Schemes, *Mon. Wea. Rev.*, 137, 991–1007,
 1015 doi:10.1175/2008MWR2556.1, 2009.

1016 Nakanishi, M. and Niino, H.: An Improved Mellor–Yamada Level-3 Model: Its Numerical
 1017 Stability and Application to a Regional Prediction of Advection Fog, *Boundary-Layer*
 1018 *Meteorol.*, 119, 397–407, doi:10.1007/s10546-005-9030-8, 2006.

1019 Oleson, K. W., Lawrence, D. M., Bonan, G. B., Flanner, M. G., Kluzek, E., Lawrence, P. J.,
 1020 Levis, S., Swenson, S. C., Thornton, P. E., Dai, A., Decker, M., Dickinson, R., Feddema, J.,
 1021 Heald, C. L., Hoffman, F., Lamarque, J. F., Mahowald, N., Niu, G. Y., Qian, T., Randerson,
 1022 J., Running, S., Sakaguchi, K., Slater, A., Stockli, R., Wang, A., Yang, Z. L., Zeng, X., and
 1023 Zeng, X.: Technical Description of version 4.0 of the Community Land Model (CLM), Tech.

1024 Rep. NCAR/TN-478+STR, National Center for Atmospheric Research, Boulder, Colorado,
 1025 USA, 2010.

1026 Prasad, A. K. and Singh, R. P.: Comparison of MISR-MODIS aerosol optical depth over the
 1027 Indo-Gangetic basin during the winter and summer seasons (2000–2005), *Remote Sensing*
 1028 *of Environment*, 107, 109–119, doi:10.1016/j.rse.2006.09.026, 2007.

1029 Qian, Y., Flanner, M. G., Leung, L. R., and Wang, W.: Sensitivity studies on the impacts of
 1030 Tibetan Plateau snowpack pollution on the Asian hydrological cycle and monsoon climate,
 1031 *Atmos. Chem. Phys.*, 11, 1929–1948, doi:10.5194/acp-11-1929-2011, 2011.

1032 Qian, Y., Yasunari, T. J., Doherty, S. J., Flanner, M. G., Lau, W. K. M., Ming, J., Wang, H.,
 1033 Wang, M., Warren, S. G., and Zhang, R.: Light-absorbing particles in snow and ice:
 1034 Measurement and modeling of climatic and hydrological impact, *Adv. Atmos. Sci.*, 32, 64–
 1035 91, doi:10.1007/s00376-014-0010-0, 2015.

1036 Qiu, J.: China: The third pole, *Nature*, 454, 393–396, doi:10.1038/454393a, 2008.

1037 Ramanathan, V. and Carmichael, G.: Global and regional climate changes due to black carbon,
 1038 *Nature Geosci*, 1, 221–227, doi:10.1038/ngeo156, 2008.

1039 Ramanathan, V., Ramana, M. V., Roberts, G., Kim, D., Corrigan, C., Chung, C., and Winker,
 1040 D.: Warming trends in Asia amplified by brown cloud solar absorption, *Nature*, 448, 575–
 1041 578, doi:10.1038/nature06019, 2007.

1042 Sarangi, C., Qian, Y., Rittger, K., Bormann, K. J., Liu, Y., Wang, H., Lin, G., and Painter, T.
 1043 H.: Impact of light-absorbing particles on snow albedo darkening and associated radiative
 1044 forcing over high-mountain Asia: high-resolution WRF-Chem modeling and new satellite
 1045 observations. *Atmos. Chem. Phys.*, 19, 7105–7128, doi:10.5194/acp-19-7105-2019, 2019.

1046 Seaman, N. L., Stauffer, D. R., and Lario-Gibbs, A. M.: A Multiscale Four-Dimensional Data
 1047 Assimilation System Applied in the San Joaquin Valley during SARMAP. Part I: Modeling
 1048 Design and Basic Performance Characteristics, *J. Appl. Meteor.*, 34, 1739–1761,
 1049 doi:10.1175/1520-0450(1995)034<1739:AMFDDA>2.0.CO;2, 1995.

1050 Shi, X., Wang, Y., and Xu, X.: Effect of mesoscale topography over the Tibetan Plateau on
 1051 summer precipitation in China: A regional model study, *Geophys. Res. Lett.*, 35, 255,
 1052 doi:10.1029/2008GL034740, 2008.

1053 Singh, P. and Bengtsson, L.: Hydrological sensitivity of a large Himalayan basin to climate
 1054 change, *Hydrol. Process.*, 18, 2363–2385, doi:10.1002/hyp.1468, 2004.

1055 Skamarock, W. C., Klemp, J. B., Dudhia, J., Gill, D. O., Barker, D. M., Duda, M., Huang, X.
 1056 Y., Wang, W., and Powers, J. G.: A Description of the Advanced Research WRF Version 3,

1057 NCAR Technical Note, NCAR/TN-468+STR, available at: <http://wrf->
1058 model.org/wrfadmin/docs/arw_v2.pdf, 2008.

1059 Stauffer, D. R. and Seaman, N. L.: Use of Four-Dimensional Data Assimilation in a Limited-
1060 Area Mesoscale Model. Part I: Experiments with Synoptic-Scale Data, *Mon. Wea. Rev.*, 118,
1061 1250–1277, doi:10.1175/1520-0493(1990)118<1250:UOFDDA>2.0.CO;2, 1990.

1062 Wagner, J. S., Gohm, A., and Rotach, M. W.: The Impact of Horizontal Model Grid Resolution
1063 on the Boundary Layer Structure over an Idealized Valley, *Mon. Wea. Rev.*, 142, 3446–
1064 3465, doi:10.1175/MWR-D-14-00002.1, 2014.

1065 Wang, X., Gong, P., Sheng, J., Joswiak, D. R., and Yao, T.: Long-range atmospheric transport
1066 of particulate Polycyclic Aromatic Hydrocarbons and the incursion of aerosols to the
1067 southeast Tibetan Plateau, *Atmospheric Environment*, 115, 124–131,
1068 doi:10.1016/j.atmosenv.2015.04.050, 2015.

1069 Wang, Y., Yang, K., Zhou, X., Chen, D., Lu, H., Ouyang, L., Chen, Y., Lazhu., and Wang, B.:
1070 Synergy of orographic drag parameterization and high resolution greatly reduces biases of
1071 WRF-simulated precipitation in central Himalaya, *Climate Dynamics*, 54, 1729–1740,
1072 doi:10.1007/s00382-019-05080-w, 2020.

1073 Wiedinmyer, C., Akagi, S. K., Yokelson, R. J., Emmons, L. K., Al-Saadi, J. A., Orlando, J. J.,
1074 and Soja, A. J.: The Fire INventory from NCAR (FINN): a high resolution global model to
1075 estimate the emissions from open burning, *Geosci. Model Dev.*, 4, 625–641,
1076 doi:10.5194/gmd-4-625-2011, 2011.

1077 Wu, G., Liu, Y., Dong, B., Liang, X., Duan, A., Bao, Q., and Yu, J.: Revisiting Asian monsoon
1078 formation and change associated with Tibetan Plateau forcing: I. Formation, *Clim Dyn*, 39,
1079 1169–1181, doi:10.1007/s00382-012-1334-z, 2012a.

1080 Wu, G., Liu, Y., He, B., Bao, Q., Duan, A., and Jin, F. F.: Thermal controls on the Asian
1081 summer monsoon, *Scientific reports*, 2, 404, doi:10.1038/srep00404, 2012b.

1082 Wu, G., Liu, Y., Zhang, Q., Duan, A., Wang, T., Wan, R., Liu, X., Li, W., Wang, Z., and Liang,
1083 X.: The Influence of Mechanical and Thermal Forcing by the Tibetan Plateau on Asian
1084 Climate, *J. Hydrometeor.*, 8, 770–789, doi:10.1175/JHM609.1, 2007.

1085 Wu, L., Su, H., and Jiang, J. H.: Regional simulation of aerosol impacts on precipitation during
1086 the East Asian summer monsoon, *J. Geophys. Res. Atmos.*, 118, 6454–6467,
1087 doi:10.1002/jgrd.50527, 2013.

1088 Wulf, H., Bookhagen, B., and Scherler, D.: Differentiating between rain, snow, and glacier
1089 contributions to river discharge in the western Himalaya using remote-sensing data and

1090 distributed hydrological modeling, *Advances in Water Resources*, 88, 152–169,
1091 doi:10.1016/j.advwatres.2015.12.004, 2016.

1092 Yang, J., Kang, S., Ji, Z., and Chen, D.: Modeling the Origin of Anthropogenic Black Carbon
1093 and Its Climatic Effect Over the Tibetan Plateau and Surrounding Regions, *J. Geophys. Res.*
1094 *Atmos.*, 123, 671–692, doi:10.1002/2017JD027282, 2018.

1095 Yasunari, T. J., Bonasoni, P., Laj, P., Fujita, K., Vuillermoz, E., Marinoni, A., Cristofanelli, P.,
1096 Duchi, R., Tartari, G., and Lau, K.-M.: Estimated impact of black carbon deposition during
1097 pre-monsoon season from Nepal Climate Observatory – Pyramid data and snow albedo
1098 changes over Himalayan glaciers, *Atmos. Chem. Phys.*, 10, 6603–6615, doi:10.5194/acp-
1099 10-6603-2010, 2010.

1100 Ye, D. Z. and Wu, G. X.: The role of the heat source of the Tibetan Plateau in the general
1101 circulation, *Meteorol. Atmos. Phys.*, 67, 181–198, doi:10.1007/BF01277509, 1998.

1102 Zängl, G., Egger, J., and Wirth, V.: Diurnal Winds in the Himalayan Kali Gandaki Valley. Part
1103 II: Modeling, *Mon. Wea. Rev.*, 129, 1062–1080, doi:10.1175/1520-
1104 0493(2001)129<1062:DWITHK>2.0.CO;2, 2001.

1105 Zaveri, R. A. and Peters, L. K.: A new lumped structure photochemical mechanism for large-
1106 scale applications, *J. Geophys. Res.*, 104, 30387–30415, doi:10.1029/1999JD900876, 1999.

1107 Zaveri, R. A., Easter, R. C., Fast, J. D., and Peters, L. K.: Model for Simulating Aerosol
1108 Interactions and Chemistry (MOSAIC), *J. Geophys. Res.*, 113, 1591,
1109 doi:10.1029/2007JD008782, 2008.

1110 Zhang, A., Fu, Y., Chen, Y., Liu, G., and Zhang, X.: Impact of the surface wind flow on
1111 precipitation characteristics over the southern Himalayas: GPM observations, *Atmospheric*
1112 *Research*, 202, 10–22, doi:10.1016/j.atmosres.2017.11.001, 2018.

1113 Zhang, R., Wang, H., Qian, Y., Rasch, P. J., Easter, R. C., Ma, P. L., Singh, B., Huang, J., and
1114 Fu, Q.: Quantifying sources, transport, deposition, and radiative forcing of black carbon over
1115 the Himalayas and Tibetan Plateau, *Atmos. Chem. Phys.*, 15, 6205–6223, doi:10.5194/acp-
1116 15-6205-2015, 2015.

1117 Zhang, R., Wang, Y., He, Q., Chen, L., Zhang, Y., Qu, H., Smeltzer, C., Li, J., Alvarado, L. M.
1118 A., Vrekoussis, M., Richter, A., Wittrock, F., and Burrows, J. P.: Enhanced trans-Himalaya
1119 pollution transport to the Tibetan Plateau by cut-off low systems, *Atmos. Chem. Phys.*, 17,
1120 3083–3095, doi:10.5194/acp-17-3083-2017, 2017.

1121 Zhang, Y., Kang, S., Cong, Z., Schmale, J., Sprenger, M., Li, C., Yang, W., Gao, T., Sillanpää,
1122 M., Li, X., Liu, Y., Chen, P., and Zhang, X.: Light-absorbing impurities enhance glacier

1123 albedo reduction in the southeastern Tibetan plateau, *J. Geophys. Res. Atmos.*, 122, 6915–
1124 6933, doi:10.1002/2016JD026397, 2017.

1125 Zhang, Y., Kang, S., Sprenger, M., Cong, Z., Gao, T., Li, C., Tao, S., Li, X., Zhong, X., Xu,
1126 M., Meng, W., Neupane, B., Qin, X., and Sillanpää, M.: Black carbon and mineral dust in
1127 snow cover on the Tibetan Plateau, *The Cryosphere*, 12, 413–431, doi:10.5194/tc-12-413-
1128 2018, 2018.

1129 Zhao, C., Chen, S., Leung, L. R., Qian, Y., Kok, J., Zaveri, R., and Huang, J.: Uncertainty in
1130 modeling dust mass balance and radiative forcing from size parameterization, *Atmos. Chem.*
1131 *Phys.*, 13, 10733–10753, doi:doi:10.5194/acp-13-10733-2013, 2013b.

1132 Zhao, C., Hu, Z., Qian, Y., Leung, L. R., Huang, J., Huang, M., Jin, J., Flanner, M., Zhang, R.,
1133 Wang, H., Yan, H., Lu, Z., and Streets, D. G.: Simulating black carbon and dust and their
1134 radiative forcing in seasonal snow: a case study over North China with field campaign
1135 measurements, *Atmos. Chem. Phys.*, 14, 11475–11491, doi:10.5194/acp-14-11475-2014,
1136 2014.

1137 Zhao, C., Huang, M., Fast, J. D., Berg, L. K., Qian, Y., Guenther, A., Gu, D., Shrivastava, M.,
1138 Liu, Y., and Walters, S.: Sensitivity of biogenic volatile organic compounds to land surface
1139 parameterizations and vegetation distributions in California, *Geosci. Model Dev*, 9, 1959–
1140 1976, doi:10.5194/gmd-9-1959-2016, 2016.

1141 Zhao, C., Liu, X., and Leung, L. R.: Impact of the Desert dust on the summer monsoon system
1142 over Southwestern North America, *Atmos. Chem. Phys.*, 12, 3717–3731, doi:10.5194/acp-
1143 12-3717-2012, 2012.

1144 Zhao, C., Liu, X., Leung, L. R., and Hagos, S.: Radiative impact of mineral dust on monsoon
1145 precipitation variability over West Africa, *Atmos. Chem. Phys.*, 11, 1879–1893,
1146 doi:10.5194/acp-11-1879-2011, 2011.

1147 Zhao, C., Liu, X., Leung, L. R., Johnson, B., McFarlane, S. A., Gustafson, W. I., Fast, J. D.,
1148 and Easter, R.: The spatial distribution of mineral dust and its shortwave radiative forcing
1149 over North Africa: modeling sensitivities to dust emissions and aerosol size treatments,
1150 *Atmos. Chem. Phys.*, 10, 8821–8838, doi:10.5194/acp-10-8821-2010, 2010.

1151 Zhao, C., Ruby Leung, L., Easter, R., Hand, J., and Avise, J.: Characterization of speciated
1152 aerosol direct radiative forcing over California, *J. Geophys. Res. Atmos.*, 118, 2372–2388,
1153 doi:10.1029/2012JD018364, 2013a.

1154 Zhao, P., Zhou, X., Chen, J., Liu, G., and Nan, S.: Global climate effects of summer Tibetan
1155 Plateau, *Science Bulletin*, 64, 1–3, doi:10.1016/j.scib.2018.11.019, 2019.

1156 Zhou, X., Beljaars, A., Wang, Y., Huang, B., Lin, C., Chen, Y., and Wu, H.: Evaluation of
1157 WRF simulations with different selections of subgrid orographic drag over the Tibetan
1158 Plateau, *J. Geophys. Res. Atmos.*, 122, 9759–9772, doi:10.1002/2017JD027212, 2017.

1159 Zhou, X., Yang, K., and Wang, Y.: Implementation of a turbulent orographic form drag scheme
1160 in WRF and its application to the Tibetan Plateau, *Climate dynamics*, 50, 2443–2455, doi:
1161 10.1007/s00382-017-3677-y, 2018.

1162 Zhao, Z., Cao, J., Shen, Z., Xu, B., Zhu, C., Chen, L. W. A., Su, X., Liu, S., Han, Y., Wang,
1163 G., and Ho, K.: Aerosol particles at a high-altitude site on the Southeast Tibetan Plateau,
1164 China: Implications for pollution transport from South Asia, *J. Geophys. Res. Atmos.*, 118,
1165 11,360–11,375, doi:10.1002/jgrd.50599, 2013.

1166 Zhong, S., Qian, Y., Zhao, C., Leung, R., Wang, H., Yang, B., Fan, Ji., Yan, H., Yang, X., and
1167 Liu, D.: Urbanization-induced urban heat island and aerosol effects on climate extremes in
1168 the Yangtze River Delta region of China, *Atmos. Chem. Phys.*, 17, 5439–5457,
1169 doi:10.5194/acp-17-5439-2017, 2017.

1170
1171
1172
1173
1174
1175
1176
1177
1178
1179
1180
1181
1182
1183

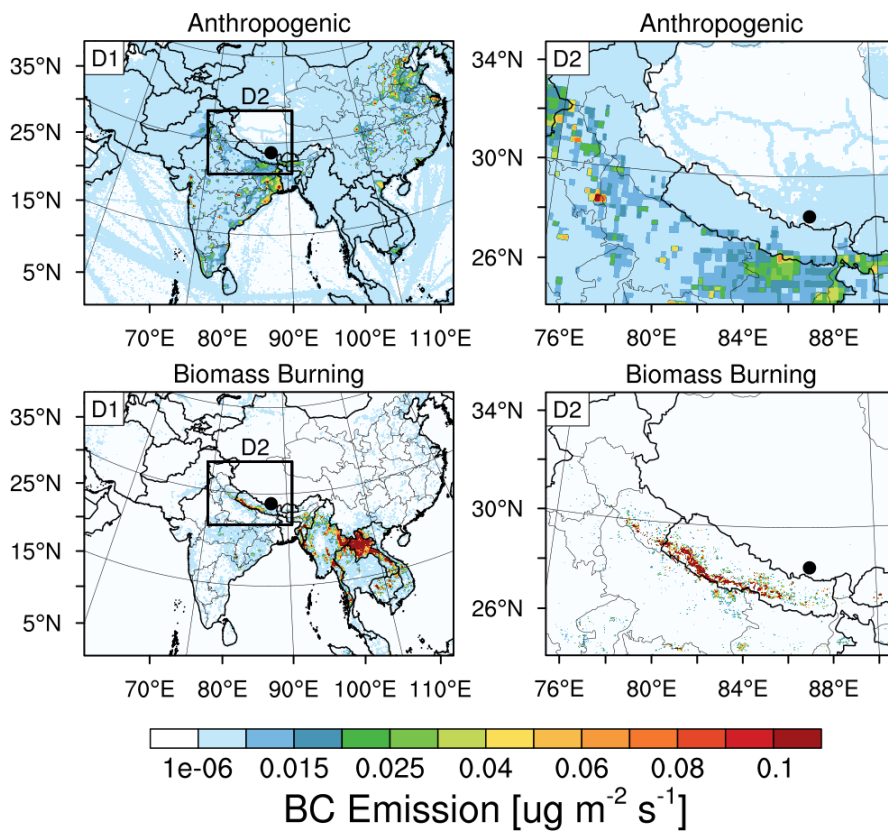
1184
 1185
 1186
 1187
 1188
 1189
 1190
 1191
 1192
 1193
 1194

Table 1. Summary of model configurations.

Description	Selection	References
Horizontal grid spacing	20 km (D1), 4 km (D2)	
Grid dimensions	250×350, 300×400	
Topography	30 arcsec (USGS)	
Vertical layers	54 (roughly 17 layers below 2 km)	
Model top pressure	50 hPa	
Nesting approach	One-way	
Aerosol scheme	MOSAIC 8 bin	Zaveri et al., 2008
Gas-phase chemistry	CBM-Z	Zaveri and Peters, 1999
Long wave Radiation	RRTMG	Iacono et al., 2000; Zhao et al., 2011, 2013a
Short-wave Radiation	RRTMG	
Cloud Microphysics	Morrison 2-moment	Morrison et al., 2009
Cumulus Cloud	Kain-Fritsch	Kain, 2004
Planetary boundary layer	MYNN level 2.5	Nakanishi and Niino, 2006
Land surface	CLM	Oleson et al., 2010
Meteorological Forcing	ERA-Interim, 0.5°×0.66°, 6 hourly	

1195
 1196
 1197
 1198
 1199
 1200
 1201
 1202
 1203
 1204
 1205
 1206
 1207
 1208
 1209
 1210
 1211
 1212
 1213

1214
1215
1216
1217
1218
1219
1220
1221
1222
1223
1224
1225



1226
1227
1228
1229
1230
1231
1232
1233
1234
1235
1236
1237
1238
1239
1240
1241
1242

Figure 1. Anthropogenic and fire emissions over the entire simulated regions of 20-km and 4-km resolutions, the black dot represents the Qomolangma Station (QOMS, 86.95°E, 28.36°N).

1243
1244
1245
1246
1247
1248
1249
1250
1251

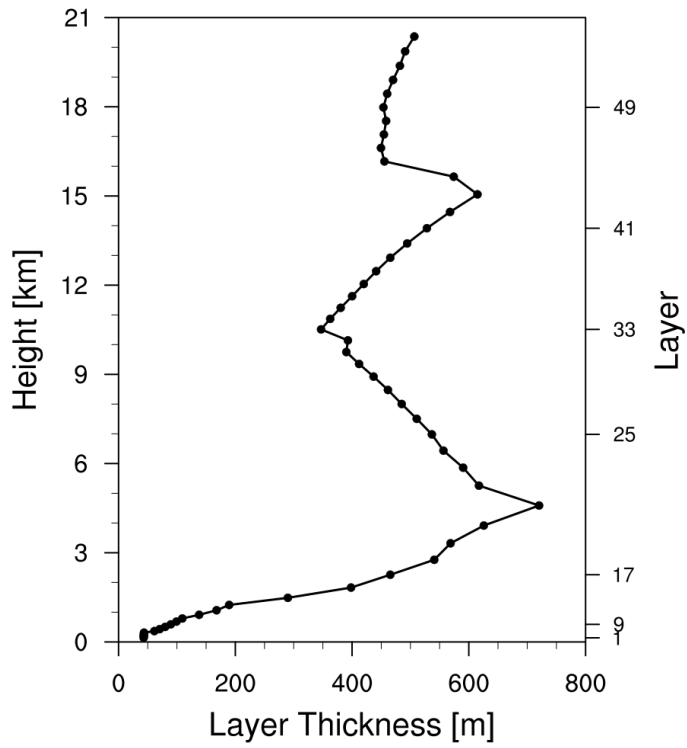
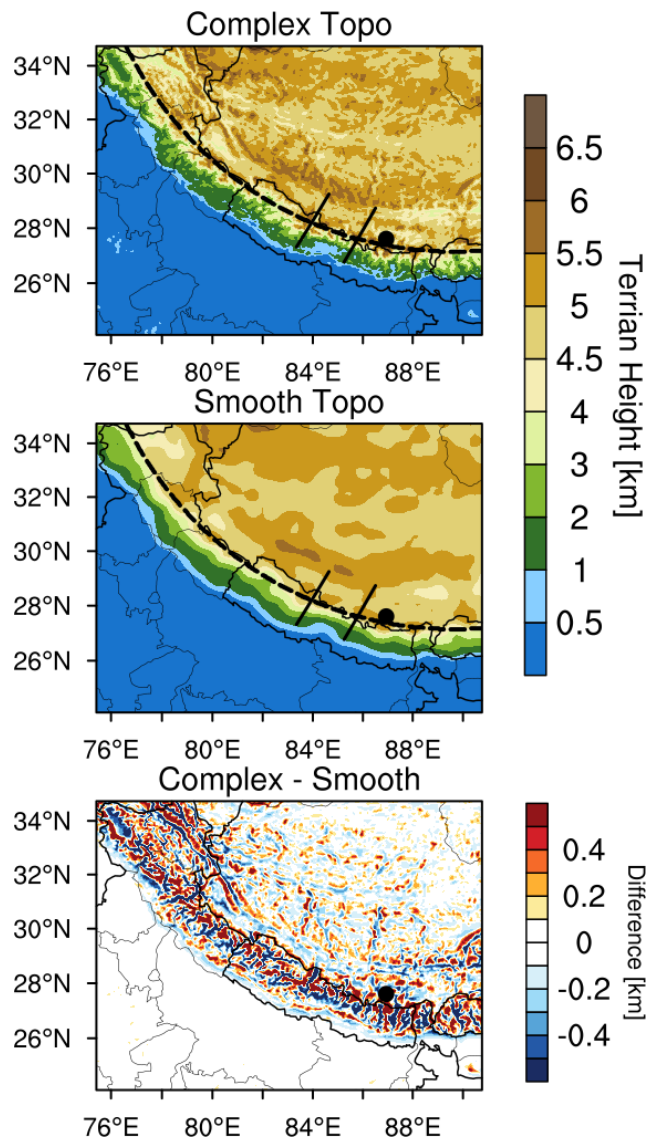


Figure 2. The thickness of each vertical layer in the simulations (54 layers in total).

1252
1253
1254
1255
1256
1257
1258
1259
1260
1261
1262
1263
1264
1265
1266
1267
1268
1269
1270
1271
1272
1273

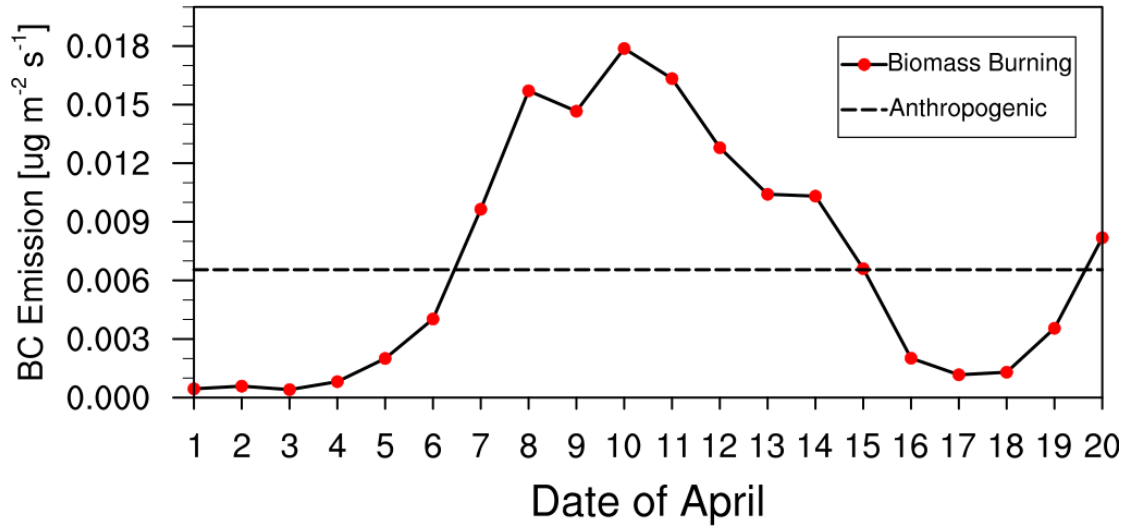
1274
1275
1276
1277
1278
1279
1280
1281
1282



1283
1284
1285
1286
1287
1288
1289
1290
1291
1292
1293

Figure 3. Spatial distributions of terrain height from the dataset at 20 km (Smooth Topo) and 4 km (Complex Topo). The one dash line and two solid lines represent the cross sections for analysis in the following.

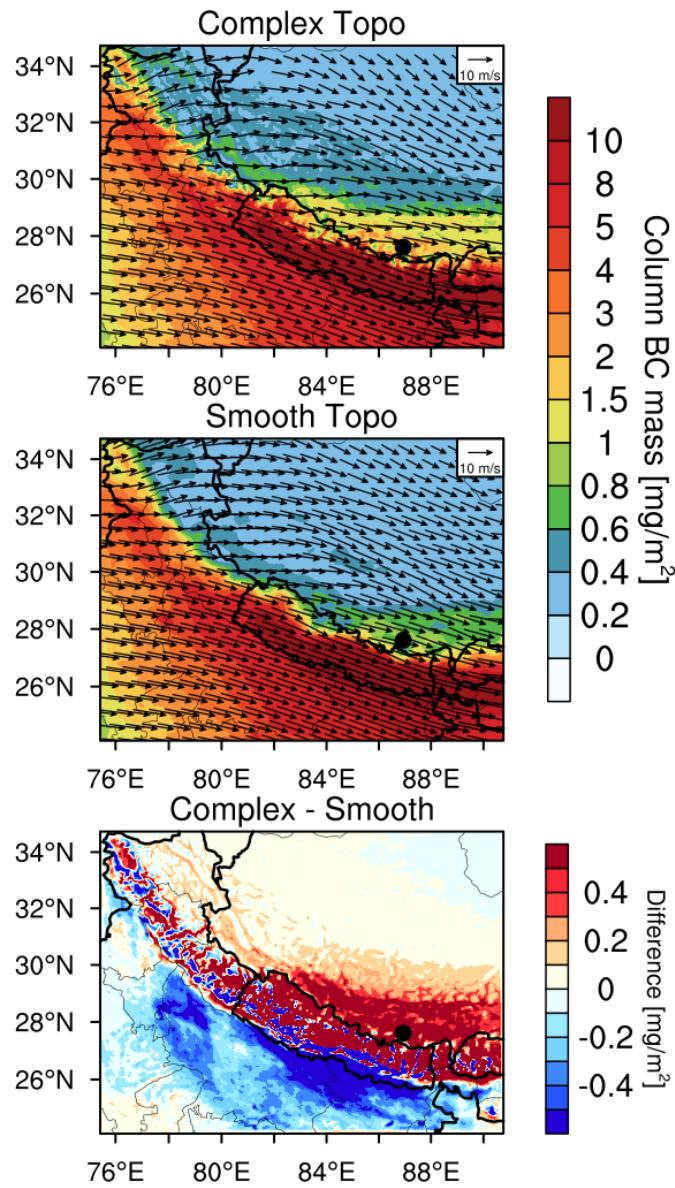
1294
1295
1296
1297
1298
1299
1300
1301



1302
1303
1304
1305
1306
1307
1308
1309
1310
1311
1312
1313
1314
1315
1316
1317
1318
1319
1320
1321
1322
1323
1324
1325
1326
1327
1328
1329
1330

Figure 4. Time series of area-averaged daily fire emissions between 26°N and 29°N over the simulation domain at 4-km resolution (The dash line in the figure represents the anthropogenic emissions).

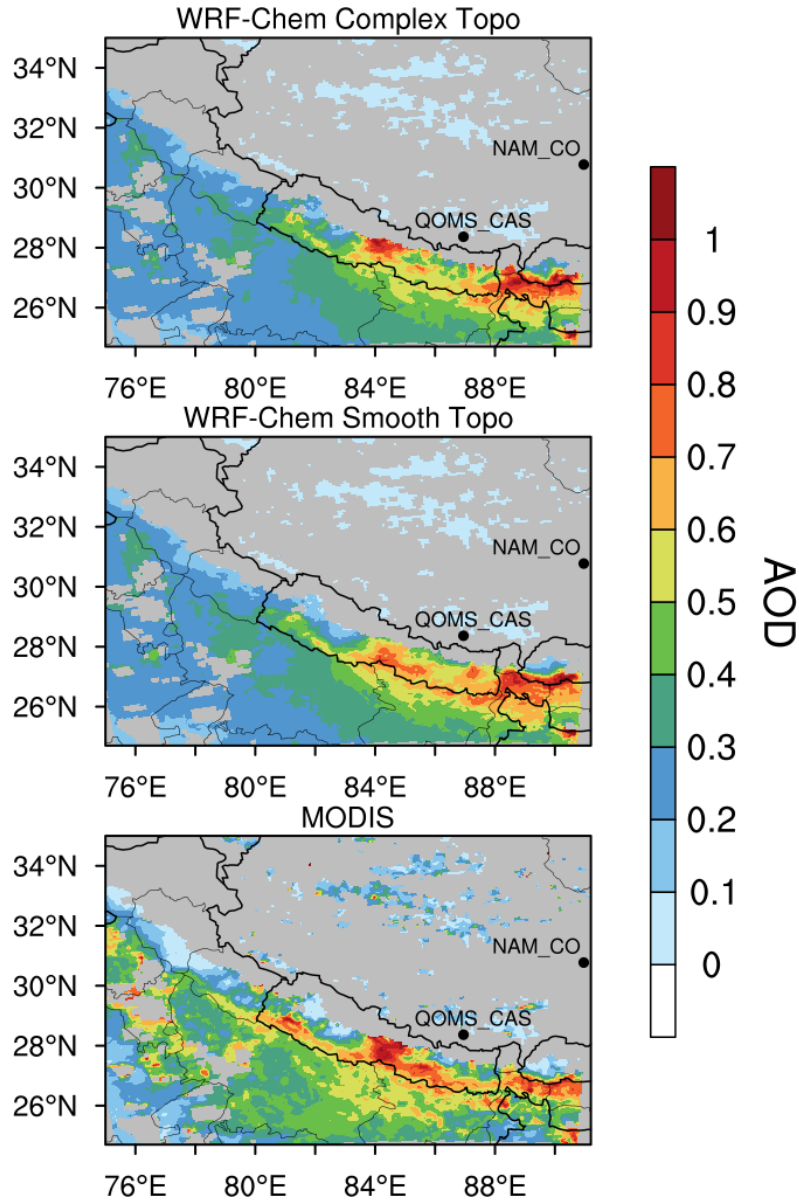
1331
1332
1333
1334



1335
1336
1337
1338
1339
1340
1341
1342
1343
1344
1345
1346
1347
1348
1349

Figure 5. Spatial distributions of column integrated BC mass and the horizontal wind field at 500 hPa from the simulations with complex and smooth topography (Complex Topo and Smooth Topo) averaged for April 1-20, 2016. The difference between the two is also shown.

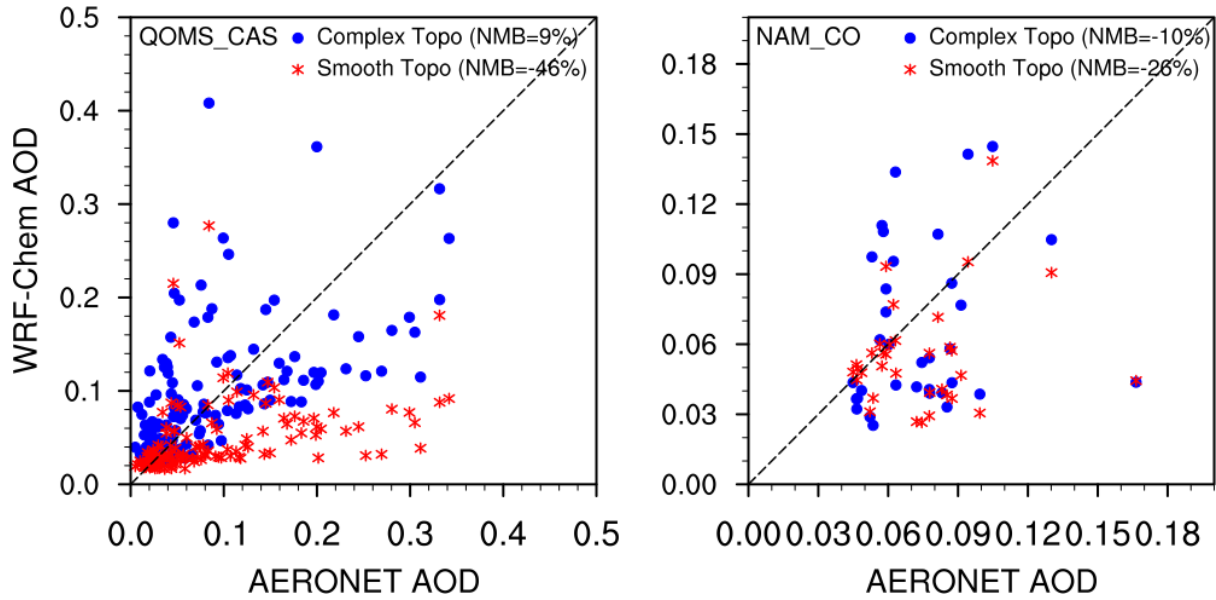
1350
1351
1352
1353
1354
1355



1356
1357
1358
1359
1360
1361
1362
1363
1364
1365
1366
1367
1368

Figure 6. Spatial distributions of AOD from the MODIS retrievals and the simulations with complex and smooth topography averaged for April 1-20, 2016. The two black dots represent the two AERONET sites over the TP (QOMS_CAS, 86.95°E, 28.36°N; NAM_CO, 90.96°E, 30.77°N).

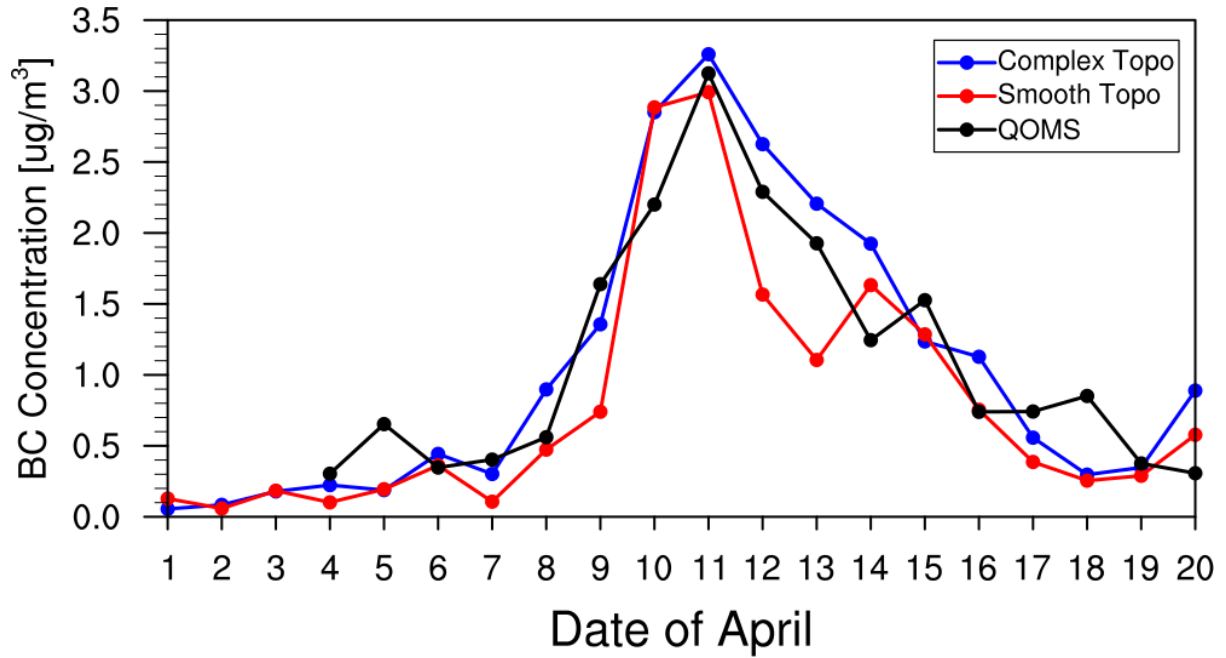
1369
1370
1371
1372
1373
1374
1375



1376
1377
1378
1379
1380
1381
1382
1383
1384
1385
1386
1387
1388
1389
1390
1391
1392
1393
1394
1395
1396
1397
1398
1399
1400
1401
1402

Figure 7. Hourly AOD from the measurements of AERONET and simulations by WRF-Chem at the two sites over the TP (QOMS_CAS, 86.95°E, 28.36°N; NAM_CO, 90.96°E, 30.77°N) for April 1-20, 2016.

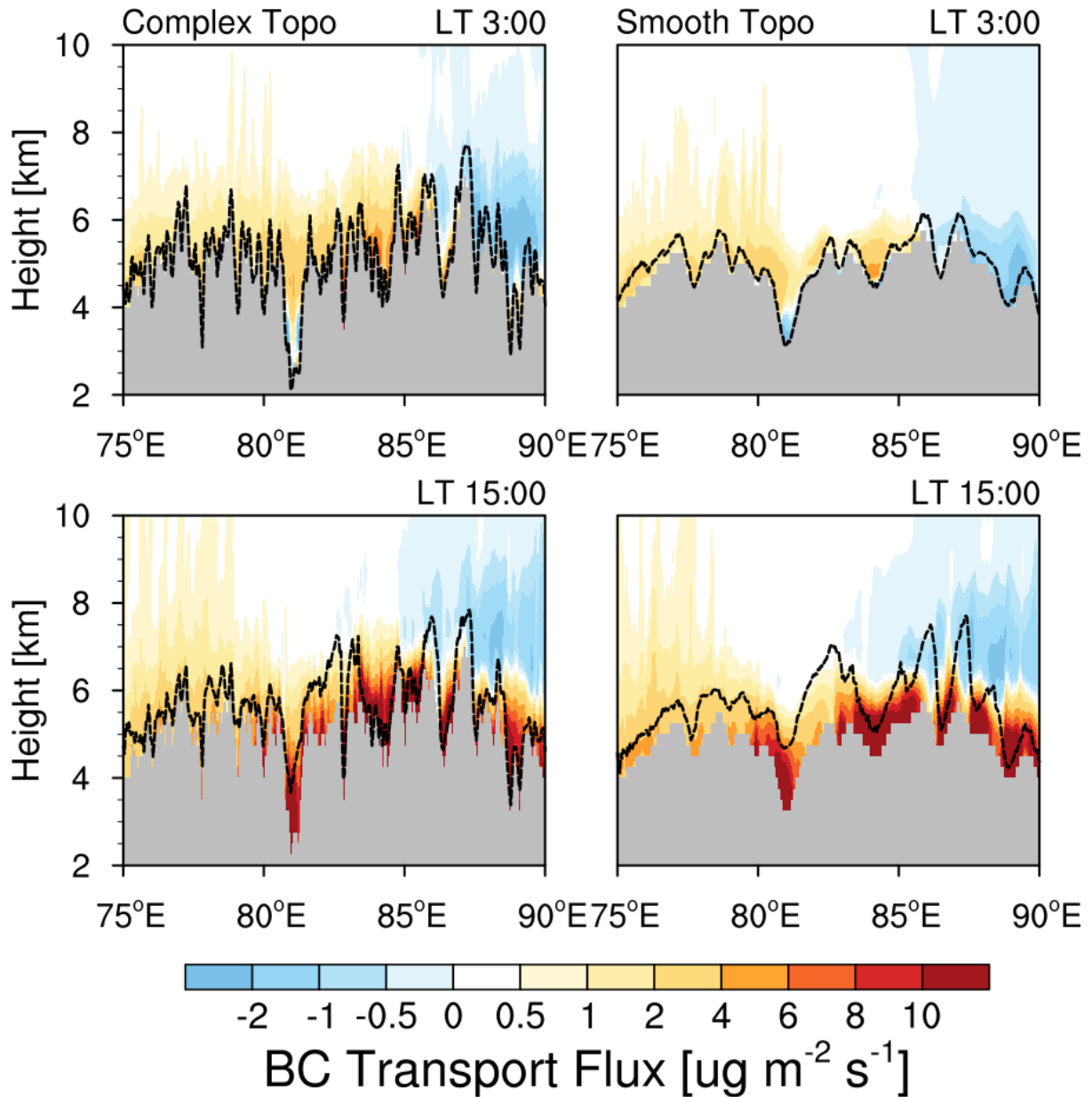
1403
1404
1405
1406
1407
1408



1409
1410
1411
1412
1413
1414
1415
1416
1417
1418
1419
1420
1421
1422
1423
1424
1425
1426
1427
1428
1429
1430
1431
1432
1433
1434
1435

Figure 8. The simulated (colored) and observed (black) temporal variability of near-surface BC mass concentration at the measurement station during April 1-20 in 2016.

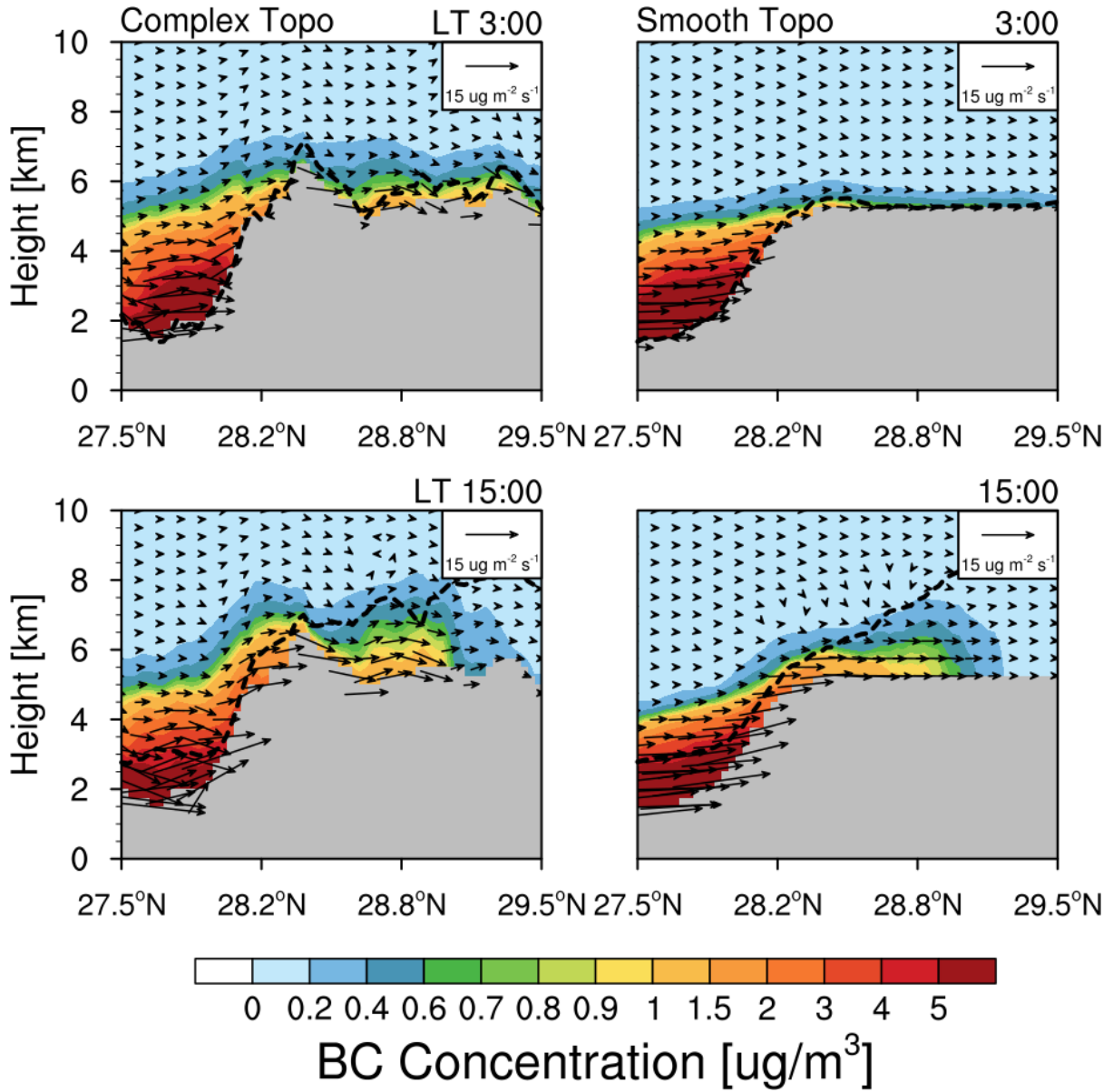
1436
1437
1438
1439
1440
1441



1442
1443
1444
1445
1446
1447
1448
1449
1450
1451
1452
1453

Figure 9. Longitude-height cross section of BC transport flux along the cross line (shown as the black dash line in Fig. 3) from the simulations with complex and smooth topography at local time (LT) 03:00 and 15:00 averaged for April 1-20. The PBL height along the cross section is shown here as the black dash line.

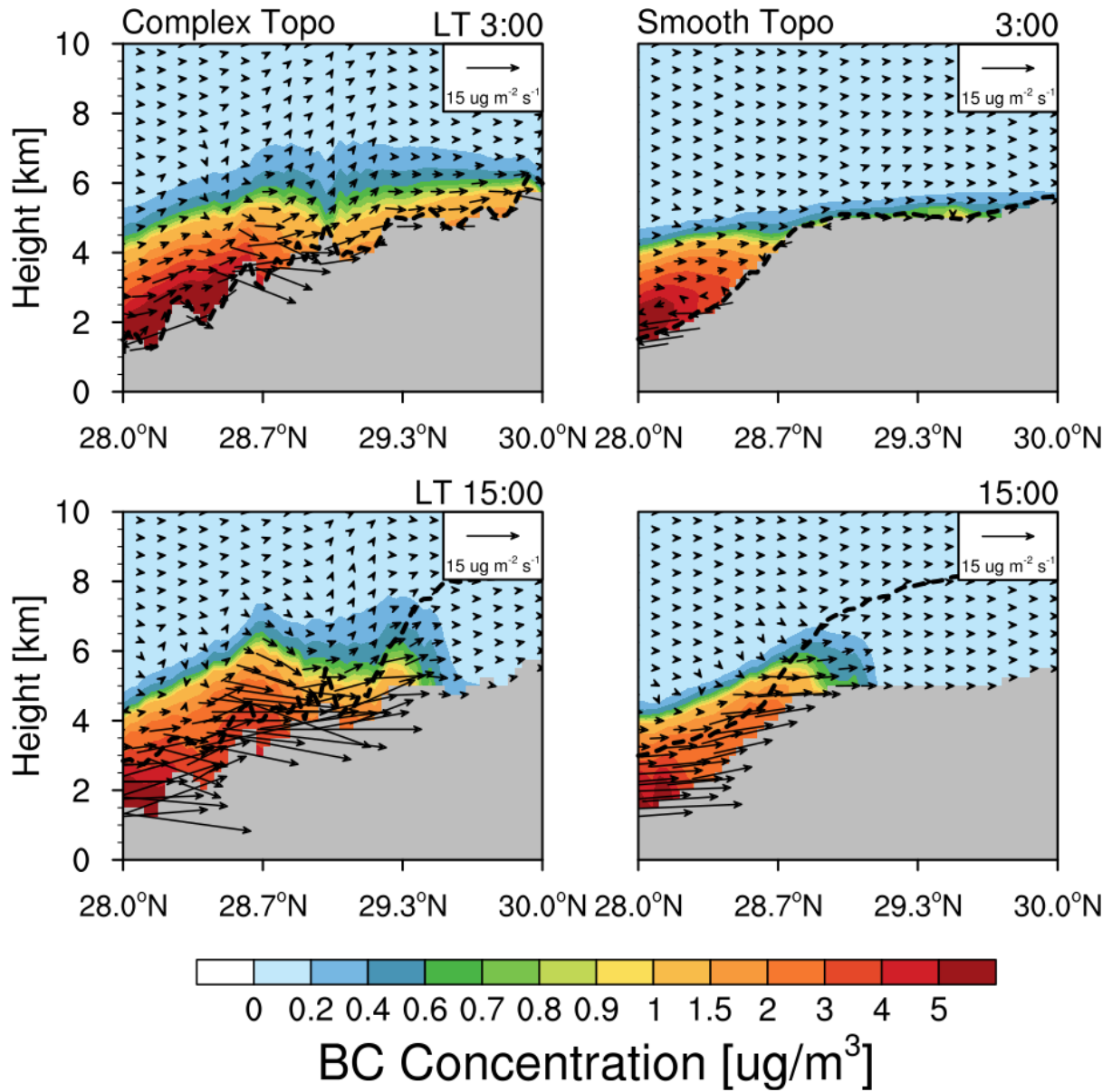
1454
1455
1456
1457
1458
1459
1460
1461



1462
1463
1464
1465
1466
1467
1468
1469
1470
1471
1472

Figure 10. Latitude-height cross section of BC flux (vector) across the mountain (shown as the East black solid line in Fig.3) from the simulations with complex and smooth topography at local time (LT) 03:00 and 15:00 averaged for April 1-20, 2016. Contour represents the BC concentration.

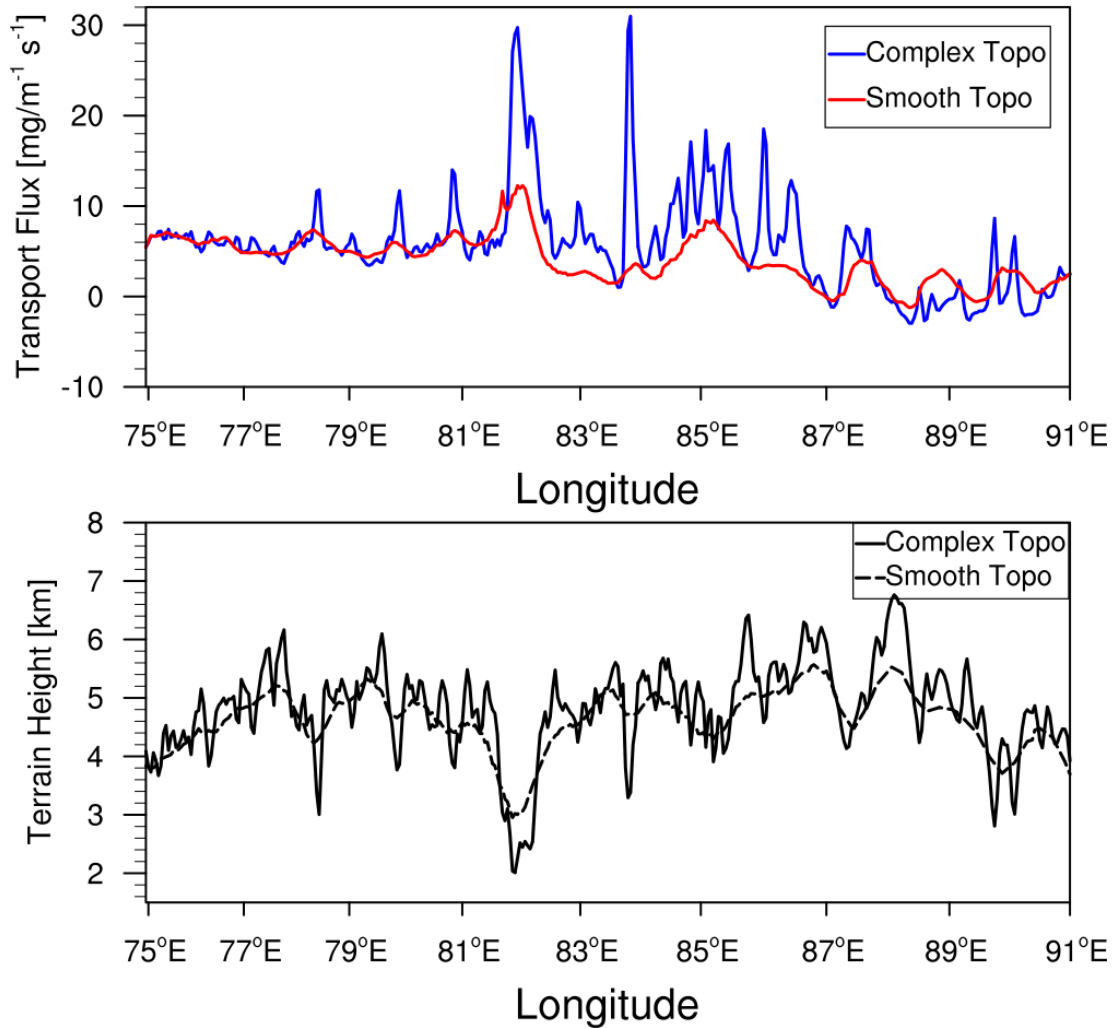
1473
1474
1475
1476
1477
1478



1479
1480
1481
1482
1483
1484
1485
1486
1487
1488
1489
1490
1491

Figure 11. Latitude-height cross section of BC flux (vector) along the valley (shown as the West black solid line in Fig. 3) from the simulations with complex and smooth topography at local time (LT) 03:00 and 15:00 averaged for April 1-20, 2016. Contour represents the BC concentration.

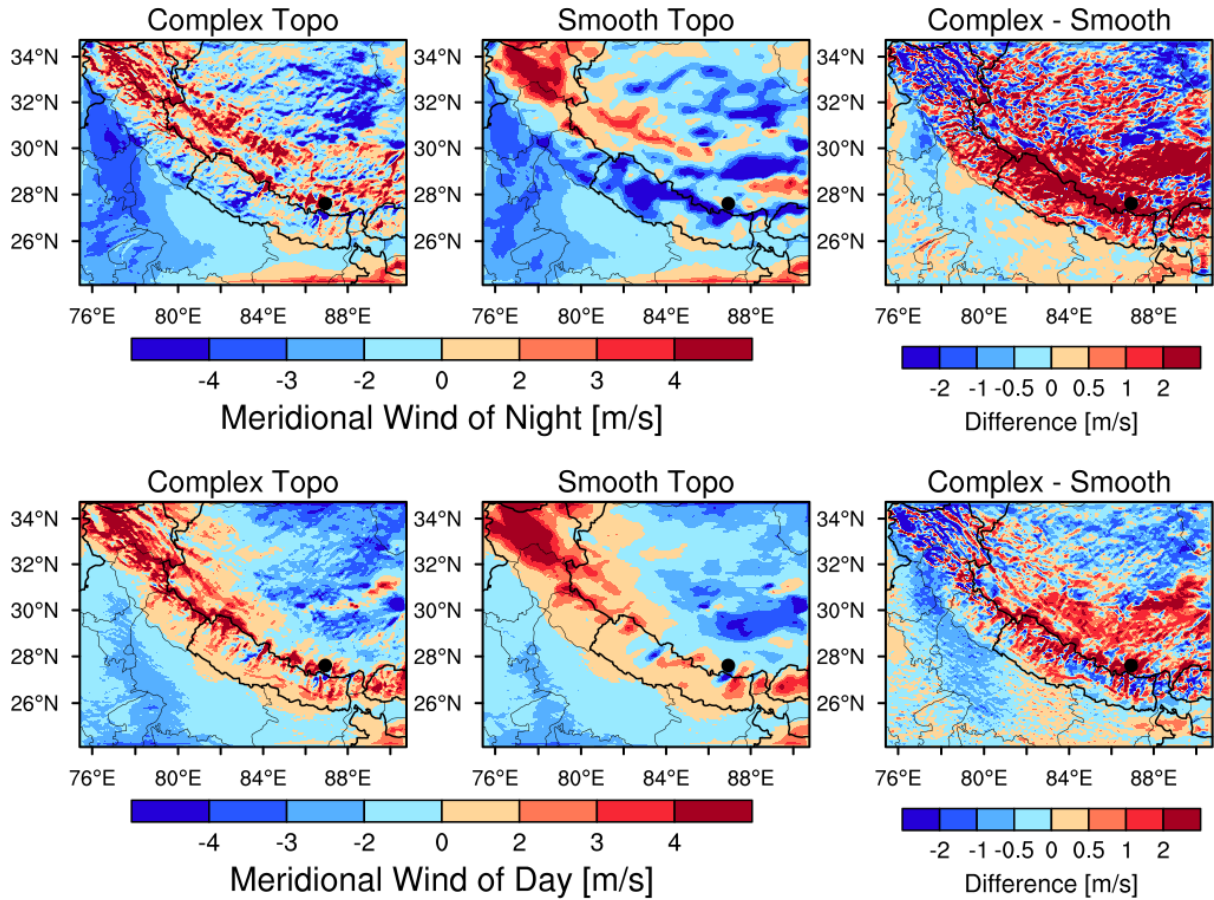
1492
1493
1494



1495
1496
1497
1498
1499
1500
1501
1502
1503
1504
1505
1506
1507
1508
1509
1510
1511
1512
1513
1514

Figure 12. Longitudinal distribution of integrated BC mass flux along the cross section in Fig. 3 from the simulations with complex and smooth topography. The black lines represent the terrain heights with different topography.

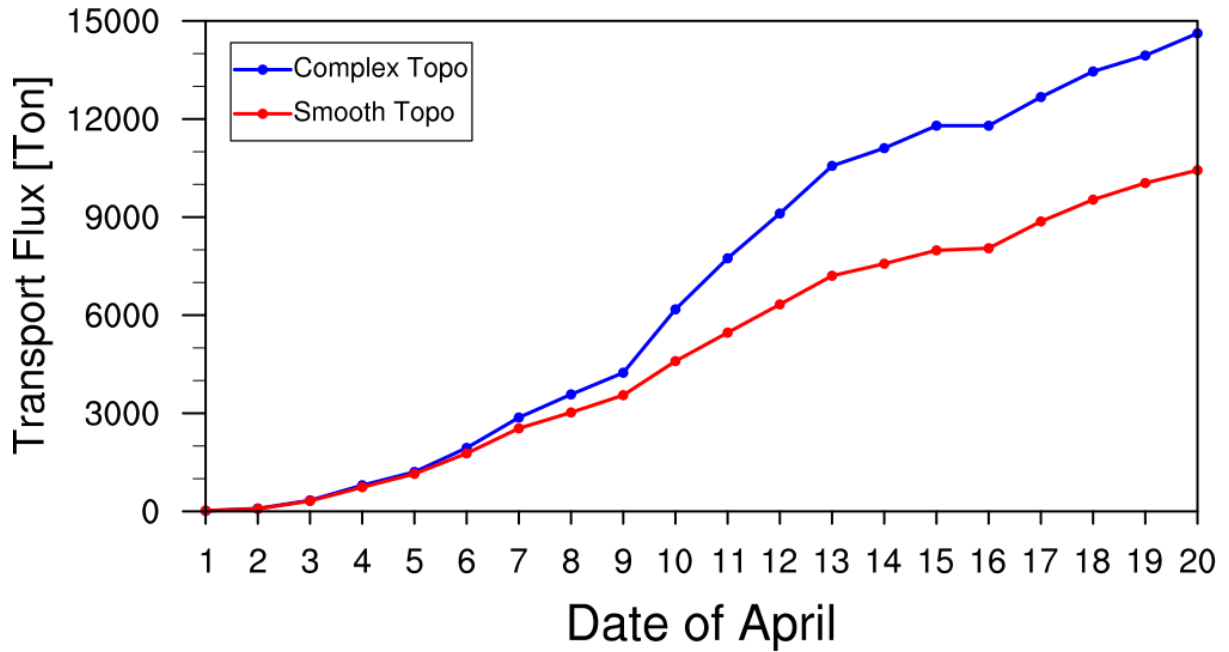
1515
1516
1517
1518
1519
1520



1521
1522
1523
1524
1525
1526
1527
1528
1529
1530
1531
1532
1533
1534
1535
1536
1537
1538
1539
1540
1541

Figure 13. Spatial distributions of meridional wind speed averaged within 500 m above the ground for day and night during April 1-20, 2016 from the simulations with complex and smooth topography. The difference between the two is also shown. Nighttime is defined as local time 21:00-6:00, and daytime is defined as 9:00-18:00. Positive value denotes southerly, and negative value denotes northerly.

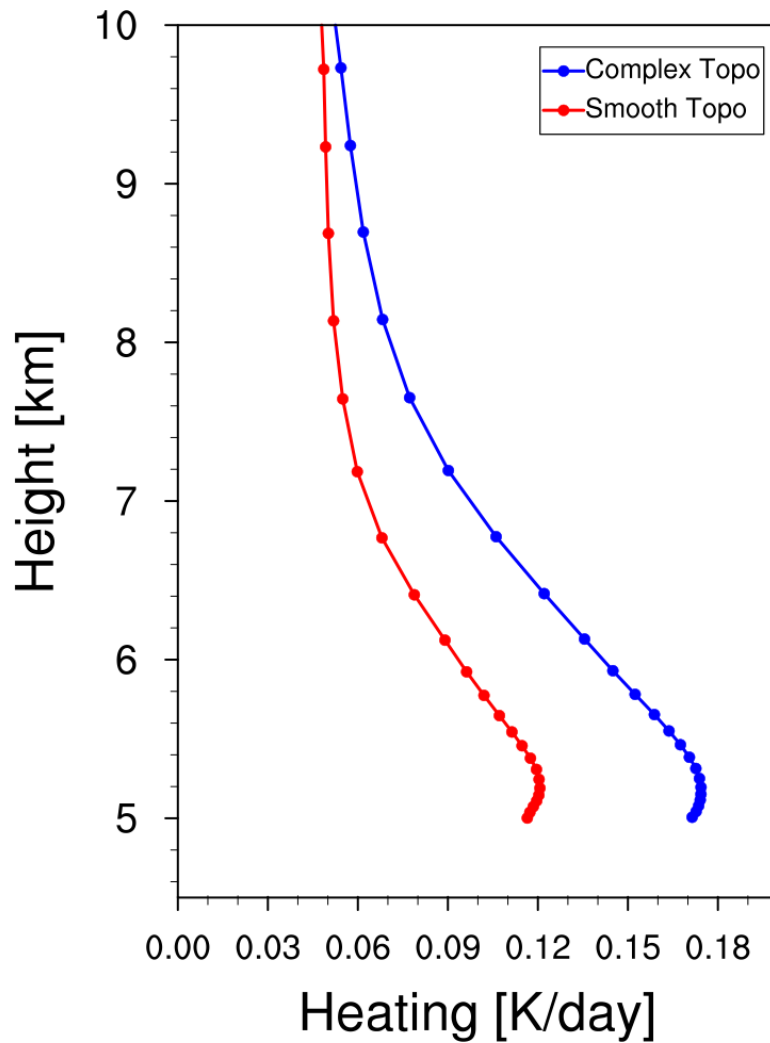
1542
1543
1544
1545



1546
1547
1548
1549
1550
1551
1552
1553
1554
1555
1556
1557
1558
1559
1560
1561
1562
1563
1564
1565
1566
1567
1568
1569
1570
1571
1572
1573
1574
1575

Figure 14. Accumulated integrated total transport flux of BC across the Himalayas estimated from the simulations with complex and smooth topography during April 1-20, 2016.

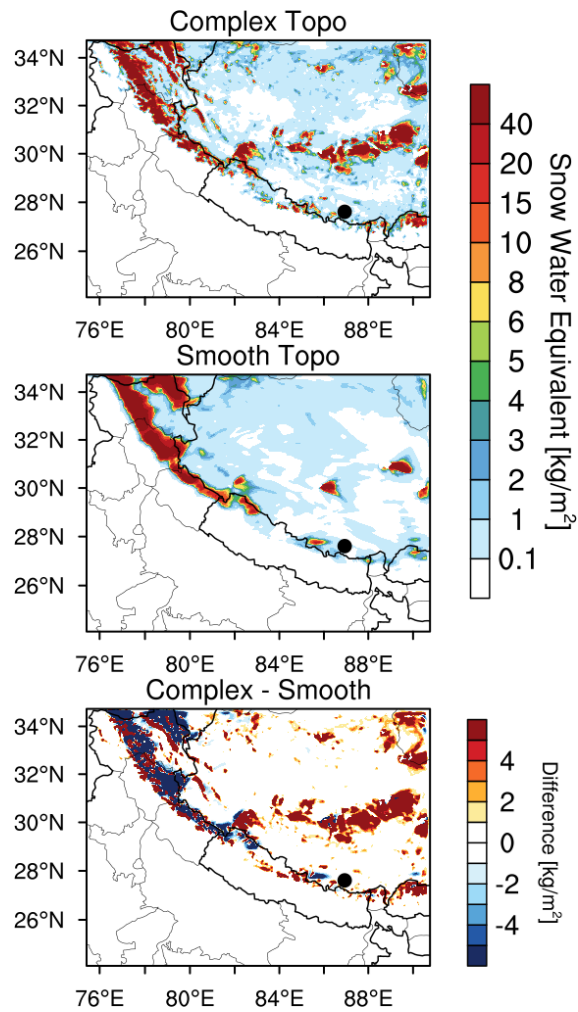
1576
1577
1578
1579



1580
1581
1582
1583
1584
1585
1586
1587
1588
1589
1590
1591
1592
1593
1594
1595
1596
1597
1598

Figure 15. Vertical profiles of BC induced radiative heating rate in the atmosphere averaged over the TP (with elevation > 4 km) from the simulations with complex and smooth topography during April 1-20, 2016.

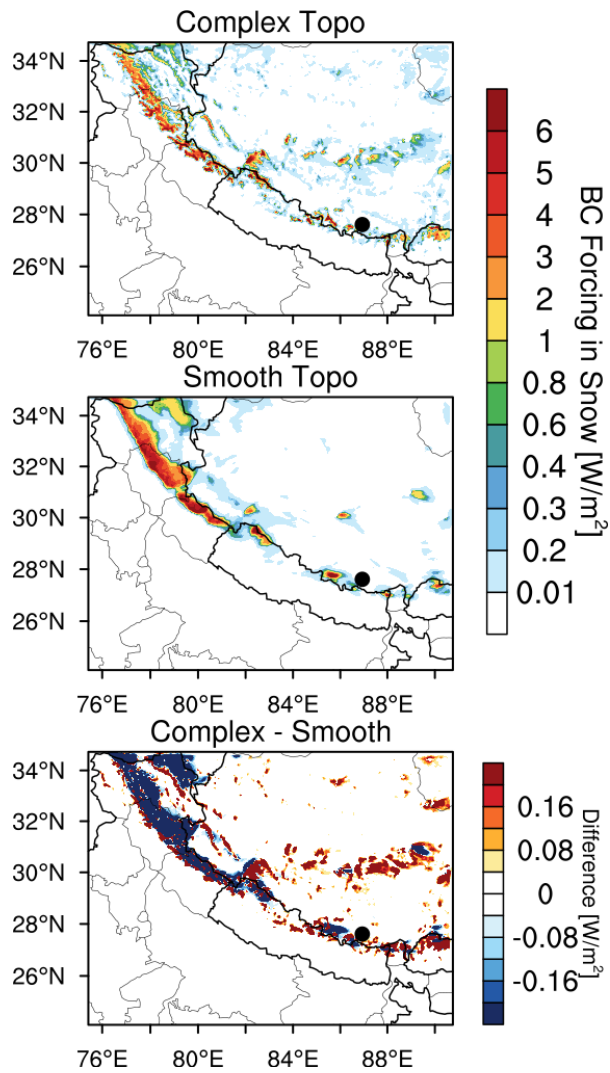
1599
1600
1601
1602



1603
1604
1605
1606
1607
1608
1609
1610
1611
1612
1613
1614
1615
1616
1617
1618
1619
1620
1621
1622

Figure 16. Spatial distributions of snow water equivalent averaged for April 1-20, 2016 from the simulations with complex and smooth topography. The difference between the two is also shown.

1623
1624
1625
1626



1627
1628
1629
1630
1631
1632
1633
1634
1635
1636
1637
1638

Figure 17. Spatial distributions of BC radiative forcing in the surface snow averaged for April 1-20, 2016 from the simulations with complex and smooth topography. The difference between the two is also shown.